Partitioning of chalcophile and highly siderophile elements (HSEs) between sulfide and carbonated melts – Implications for HSE systematics of kimberlites, carbonatites, and melt metasomatized mantle domains

Proteek Chowdhury [a,b*], Rajdeep Dasgupta [b], Patrick R. Phelps [b], Cin-Ty A. Lee [b] and Ryan A. Anselm [b,c]

[a] *Department of Earth and Planetary Sciences, University of California Riverside, Riverside, CA 92521, USA*

[b] *Department of Earth, Environmental and Planetary Sciences, Rice University, 6100 Main Street, MS 126, Houston, TX 77005, USA*

[c] *Clements High School, 4200 Elkins Road, Sugarland, TX 77479, USA*

Abstract

Highly Siderophile Elements (HSEs; Os, Ru, Ir, Rh, Pt, Pd, Au and Re) combined with their isotopic systematics (Re-Os and Pt-Os) are powerful tools for tracking evolution and genesis of mantle derived magmas. Given sulfides (accessory sulfide minerals and/or molten sulfides) are the primary hosts of HSEs in the mantle and low-degree carbonated melts are extracted from large portions of mantle volume, partitioning of HSEs between sulfide and carbonated melt might play a critical role in distributing HSEs between the mantle and crustal reservoirs. Although, partitioning of HSEs and chalcophile elements between sulfide melt and silicate melt has been previously studied, partitioning of these elements between sulfide melt and carbonated melts has not received much attention. Here we use high *P*-*T* experiments to determine the partitioning of HSEs and chalcophile elements (Ni, Co, Mo, Os, Ru, Pd, Pt and Re) between (i) sulfide melt and carbonated silicate melt (CO_2~17 wt.%) and (ii) sulfide melt and carbonatitic melt (CO_2~ >30 wt. %) at a pressure (*P*) of 3 GPa and temperatures (*T*) of 1300-1600 °C in graphite capsules. All experiments produced quenched Fe-sulfide melt blobs + carbonated silicate melt matrix. Concentrations of major elements were measured using electron microprobe, and HSEs and chalcophile elements were measured using LA-ICP-MS. We find that all the elements measured are compatible in the sulfide melt to varying degrees and their $D^{\text{sulfide/carb. melt}}$ sequence is Mo < Co < Ni < Re < Pt ≤ Pd < Ru ≤ Os varying from around 10 for Mo to 10^5 for Os. Comparing the $D^{\text{sulfide-carb. melt}}$ with $D^{\text{sulfide-silicate}}$ from previous studies, we show that the partition coefficients of HSEs between sulfide and carbonated melts are lower than the partition coefficients of these elements between sulfide and silicate melts, indicating greater mobilization of these elements in carbonatites and carbonated silicate melts. Calculating bulk D ($\overline{\overline{D}}$) for carbonated peridotite using our experimentally measured *D* values, we model the HSE contents of mantle derived low-degree

partial melts using an aggregate fractional melting equation and compare the primitive mantle normalized HSE patterns of our model with natural kimberlites, carbonatites, ocean island basalts, and alkaline basalts. We also calculate proportions of sub-lithospheric continental mantle (SCLM) xenolith detritus in the natural kimberlite and carbonatite samples from Karelian, Kaapvaal, Canadian shield and North China craton by using mass balance calculations based on Ru concentration in the primary carbonated melt and the SCLM xenoliths. Our calculations show that detritus proportion in natural kimberlites are 2-28% for Karelian, 7-28% for Kaapvaal, and 6-16% for Canadian shield, which are in agreement with previous studies using various other proxies. We also show that the extent of Re/Os fractionation is less for events of carbonate melt metasomatism as compared to similar events of basaltic melt metasomatism.

Keywords: Highly Siderophile Elements (HSE); sulfide; carbonatite; kimberlite; partition coefficients; mantle xenoliths.

1. INTRODUCTION

Sulfur (S) is one of the crucial multi-valent, volatile elements on Earth. The deep Earth sulfur reservoir is controlled by melting-induced extraction and degassing of sulfur at plate boundaries (e.g. Wallace and Edmonds, 2011; Ding and Dasgupta, 2017), convergent boundaries (e.g. Alt et al., 1993; Chowdhury and Dasgupta, 2019; Li et al., 2020), intraplate ocean islands (e.g. Brounce et al., 2017; Ding and Dasgupta, 2018; Moussallam et al., 2019), and subduction of sulfides or sulfates back to deep Earth (Jégo and Dasgupta, 2013; Jégo and Dasgupta, 2014; Tomkins and Evans, 2015; Canil and Fellows, 2017; Walters et al., 2020). In deep terrestrial mantle, sulfur is primarily stored as accessory sulfide phases, either as solid or molten sulfide solutions (e.g. Harvey et al., 2016). These sulfides are the major host of chalcophile elements (Cu, Ni, Co, Mo etc.), Platinum Group Elements (PGEs - Os, Ir, Ru, Rh, Pt and Pd), and Highly Siderophile Elements (HSEs - PGEs, Re and Au) (Brenan, 2008; Lorand et al., 2013; Mungall and Brenan, 2014). To understand the formation and evolution of mantle derived rocks such as mid-ocean ridge basalts (MORB - Rehkämper et al., 1999; Bézos et al., 2005), ocean island and alkalic basalts (Day et al., 2010; Day, 2013; Day, 2013; Gannoun et al., 2015), komatiites (Puchtel and Humayun, 2001), kimberlites (Tappe et al., 2017; Maier et al., 2017), and carbonatites (Ackerman et al., 2019; He et al., 2020) HSE geochemistry along with Re-Os and Pt-Os isotopic systematics has been used because of the strong partitioning of these elements into accessory sulfides and metallic phases co-existing with silicates and carbonated melts. Also, as the HSEs fractionate during partial melting of the mantle through Earth's history, there is variability of distribution of these elements in the mantle and crustal reservoirs (Barnes et al., 1985; Mondal, 2011). Hence, HSE partitioning during mantle melting is a crucial parameter in understanding how HSE concentrations vary in different reservoirs and as a function of different melt compositions.

Because HSEs and chalcophile elements are mostly concentrated in the sulfide phases in the mantle, a number of laboratory experiments and analysis of natural samples have explored the sulfide-silicate melt partition coefficients for HSEs ($D_{\text{HSE}}^{\text{Sulfide-silicate}}$) and chalcophile elements ($D_{\text{Chalcophile elements}}^{\text{Sulfide-silicate}}$), with estimated values ranging from 10 to 10^8 (e.g. Peach et al., 1990; Fleet et al., 1996; Crocket et al., 1997; Pruseth and Palme, 2004; Fonseca et al., 2009; Li and Audétat, 2012; Kiseeva and Wood, 2013; Patten et al., 2013; Mungall and Brenan, 2014). These studies constrained the *D* values and used these values to understand HSE and chalcophile element systematics in upper mantle melting conditions such as beneath mid-ocean ridges (Li and Audétat, 2012; Kiseeva and Wood, 2013; Mungall and Brenan, 2014) and beneath arc volcanoes (Li and Audétat, 2012). However, partitioning of these elements between sulfide and carbonated melts ($D_{\text{HSE}}^{\text{Sulfide-carb. melt}}$ and $D_{\text{Chalcophile elements}}^{\text{Sulfide-carb.melt}}$) has not received much attention (Jorgenson, 2017) in spite of bulk portion of Earth's sulfide saturated mantle beneath oceans and continents being affected by CO_2±H_2O induced melting (Dasgupta et al., 2013; Moussallam et al., 2015; Dasgupta, 2018) and extraction of deep carbonated melts (e.g., Keller et al., 2017). The deepest melts beneath mid-oceanic ridges, depending on the oxygen fugacity of the mantle (e.g., Gaillard et al., 2015; Eguchi and Dasgupta, 2018), are thought to be carbonatitic, which evolves to carbonated silicate melts at shallower depths (Dasgupta et al., 2007b; Dasgupta et al., 2007a; Dasgupta and Hirschmann, 2010; Dasgupta et al., 2013; Poli, 2015; Sun and Dasgupta, 2019). The first generated melt at sub-continental lithospheric mantle (SCLM) is also thought to be silica undersaturated carbonated silicate melt if the mantle oxygen fugacity is as reduced as sampled by continental mantle xenoliths (Frost and McCammon, 2008; Stagno and Frost, 2010; Stagno et al., 2013). Coexisting with carbonated silicate melt at these conditions, the stable sulfur-bearing phase is

again thought to be molten sulfides (Chowdhury and Dasgupta, 2020). The effect of carbonated melt metasomatism on the HSE systematics has been studied extensively (Lorand et al., 2004; Alard et al., 2011; Aulbach et al., 2014; Burness et al., 2020) and there is some previous work on HSE concentrations of carbonatites and kimberlites (Xu et al., 2008; Maier et al., 2017; Ackerman et al., 2019; He et al., 2020) along with their Re-Os isotopic systematics (Ackerman et al., 2019; He et al., 2020). All these previous studies used $D_{\mathrm{HSE}}^{\mathrm{Sulfide-silicate}}$ in part based on the assumption that sulfide-silicate melt vs sulfide-carbonated melt elemental partitioning may be similar and in part owing to the lack of any partitioning experiments of HSEs between sulfide and carbonated silicate melts. However, the structure of basaltic melt and strongly carbonated melts that are parental to natural carbonatite and kimberlite are quite different, with strongly ionic clusters in the latter (e.g., Vuilleumier et al., 2015; Ghosh et al., 2017). The strong difference in melt structure with very different extent of polymerization may lead to distinctly different elemental partitioning in sulfide-silicate melt vs sulfide-carbonated melt systems. Hence, the partitioning of HSEs and chalcophile elements between sulfide and carbonated melt need to be constrained to understand the systematics of these elements in mantle derived carbonatites and carbonated silicate (kimberlitic) melts as well as in mantle domains that experience carbonated melt metasomatism.

In certain areas like Phalaborwa, South Africa (Eriksson, 1989; Le Bras et al., 2020), and Ipanema, Brazil (Fontana, 2006), there are carbonatite-phoscorite complexes, which are thought to contain considerable amounts of HSEs, making them a potential source of these elements for mineral exploration. There are several other studies which suggest large scale HSE deposits are more likely to form in cratonic large igneous provinces (LIPs) instead of off-cratonic LIPs as cratonic carbonated magmas can partially dissolve PGEs while ascending through SCLM (Zhang et al., 2008; Griffin et al., 2013; Burness et al., 2020), but to understand the HSE concentrations

and its systematics in the cratonic carbonated silicate magmas, constraints on partitioning of these elements between sulfide and carbonated melts are required at mantle conditions.

Here we experimentally determine the partitioning of 8 HSEs and chalcophile elements (Ni, Co, Mo, Os, Ru, Pd, Pt and Re) between (i) sulfide melt and carbonated silicate melt (CO_2~17 wt.%] and (ii) sulfide melt and carbonatitic melt (CO_2~ >30 wt.%) at a single pressure (P) of 3 GPa and temperatures (T) of 1300-1600 °C. The $D^{\text{sulfide/carb. melt}}$ values for systems comprising two different melt compositions (low- and high-CO_2) were used to calculated bulk Ds ($\overline{\overline{D}}$) for carbonated peridotite (garnet lherzolite, dunite, and wehrlite). The HSE content of low-degree partial melts were calculated using the aggregate fractional melting model and our estimated bulk Ds. Through comparison of natural kimerlite and carbonatite HSE inventories and our modeled primary melts, we calculate the proportion of xenolith detritus in the natural kimberlites and carbonatites that are necessary for various localities such as Karelian, Kaapvaal, Canadian shield, and North China craton. We suggest that for different cratons, varying proportions of these detritus SCLM materials need to get incorporated, modifying the original HSE contents of primary kimberlitic and carbonatitic melts. We also discuss how the metasomatic signature of carbonatitic vs basaltic melt is expected to differ, in terms of Re/Os systematics, if they derive from sulfide-bearing mantle.

2. METHODS

2.1. Starting compositions

The starting compositions are two carbonated silicate melts with very different CO_2 contents similar to the study by Chowdhury and Dasgupta (2020) and are reported in Table 1. The lower CO_2 composition [~17 wt.%; CSL1 of Chowdhury and Dasgupta (2020)] is a carbonated silicate

140 melt from an experiment by Dasgupta et al. (2013) and the one with higher CO_2 [~31 wt.%; CSL2
141 of Chowdhury and Dasgupta (2020)] is a carbonatitic melt from the study of Sun and Dasgupta
142 (2019). The carbonated melts were prepared using reagent grade oxides (SiO_2, TiO_2, Al_2O_3, MgO,
143 Fe_2O_3, MnO_2) and carbonates ($CaCO_3$, K_2CO_3, Na_2CO_3), and natural dolomite. To avoid
144 adsorption and incorporation of surrounding water in the starting mixes, SiO_2, TiO_2, Al_2O_3 and
145 MgO were heated overnight at 1000 °C, Fe_2O_3 at 800 °C, MnO_2 at 400 °C, $CaCO_3$ at 200 °C and
146 K_2CO_3 and Na_2CO_3 at 110 °C. Starting materials for sulfides consists of a stoichiometric FeS
147 doped with lithophile, HSEs, and chalcophile elements. HSEs and chalcophile elements were
148 added from a mix of 21 elements (Cu, Pb, Ag, Mn, Zn, Cr, Sb, Bi, V, Sc, Ga, Ge, Te, Ni, Co, Mo,
149 Os, Ru, Pd, Pt and Re) prepared from pure metals and oxides which were mixed in agate mortar
150 and pestle. Sulfides were doped with the trace element mix introducing ~500-7000 ppm of each
151 element. Thereafter, homogeneous mixtures of carbonated melt mix and the doped sulfides (FeS)
152 in a 9:1 mass ratio were prepared using a mortar and pestle under ethanol and stored in a drying
153 oven at 120 °C.

154 **2.2. Experimental technique**

155 The experiments were performed using an end-loaded piston cylinder (PC) apparatus at the
156 Experimental Petrology Laboratory of Rice University at a pressure of 3 GPa and temperatures of
157 1300 - 1600 °C. The half-inch PC assembly consisted of $BaCO_3$ pressure medium, crushable MgO
158 spacers, and straight-walled graphite heater, all contained in a Pb foil for housing friable $BaCO_3$
159 assembly and to minimize friction in the experimental assembly. The pressure and temperature
160 calibration of this assembly are detailed in Tsuno and Dasgupta (2011). To monitor and control
161 the temperature of the PC experiments a type-C thermocouple oriented axially with respect to the
162 heater and located next to the capsule was used. Pressure and temperature uncertainties are

estimated to be ± 0.1 GPa, ±10 °C based on the *P-T* calibration of Tsuno and Dasgupta (2011). Thick walled (~2-2.5mm) graphite capsules were used as containers for the starting mixes. In all experiments, two different compositions were loaded into a multi-chambered graphite container with two 1.5-2 mm diameter holes. In all experiments the graphite capsules were placed in the hotspot of the PC assembly. After initial pressurization to the target pressure at room temperature, all experiments were heated to 800 °C at a heating rate of 100 °C/min and sintered for 2-4 hours to reduce the porosity in graphite capsule, which is known to prevent migration of sulfide-rich melt through graphite (Buono and Walker, 2011; Buono et al., 2013; Tsuno and Dasgupta, 2015). After the sintering step, the experiments were raised to the nominal target temperatures of 1300-1600 °C, at a heating rate of 100 °C/min. The experiments were held at the target *P-T* for 8-24 h and terminated by cutting off power to the heater after keeping for the desired duration. The lower temperature experiments were run longer. The assemblies were slowly depressurized and the retrieved graphite capsules were mounted in epoxy and ground transversely using 600-1200 grit silicon carbide strip grinders until the top of the sample chambers were visible; the subsequent grinding and polishing of the samples were done on dry nylon and velvet microcloth using 1–3 μm diamond powders. Because we used multi-chambered graphite containers, we didn't cut open the container longitudinally where there was a possibility of losing one sample. Thus, we are unable to report the residual silicate phases expected to be present in the lower temperature experiments (Chowdhury and Dasgupta, 2020), because they stabilize in the cooler, bottom ends of the piston cylinder experiments.

2.3. Analytical techniques

2.3.1. Electron probe micro analysis (EPMA)

Polished samples were carbon-coated and investigated using a JEOL JXA 8530F Hyperprobe at the Rice University for phase identification using energy dispersive spectroscopy (EDS), for textural relationship among phases using backscattered electron (BSE) images, and for obtaining major element abundances and S content of nominally S-bearing phases using WDS spectroscopy. Analyses were performed using a 15 kV (accelerating voltage), 10 nA (beam current) electron beam with spot size of 20-40 μm for carbonated and sulfide-rich melt pools and focused spot size on residual silicate mineral grains. The peak counting times were 10 s, whereas the background counting times were 5s for all the elements, including sulfur. Analytical standards included natural basaltic glass (NMNH-113716; for Na, Si, Mg, Al, K, Mn and S), olivine (for Fe), rutile (for Ti), and grossular (for Ca). A Smithsonian basaltic glass standard (USNM 111240) was also used as a secondary standard for all elements, including S.

2.3.2. LA-ICP-MS Analysis

Concentrations of Co, Ni, Mo, Ru, Pd, Re, Os and Pt in the carbonated melt and sulfides were determined using laser ablation inductively coupled plasma mass spectrometry (LA-ICP-MS) at Rice University using a ThermoFinnigan Element 2 magnetic sector mass spectrometer equipped with a New Wave 213 nm laser ablation system. The standard reference material for the laser ablation analyses were synthetic glasses, HOBA, NIST 610, and NIST 612. HOBA, which is an iron meteorite (Campbell and Humayun, 2005), was used for analyzing the HSEs, whereas NIST 610 and 612 was used for Co, Ni, and Mo. All the other elements used in doping our starting mix was not analyzed due to unavailability of appropriate sulfide standard in our laboratory. To account for different yields during ablation, ^{57}Fe was used as the internal standard for sulfide melts, whereas ^{43}Ca was used as the internal standard for carbonated melts.

209 The synthetic glass and meteorite standards and the experimental sulfide and carbonated melts
210 were ablated using spot analyses. 25 μm diameter spots were used for sulfide melt blobs and 80
211 μm diameter spots were used for carbonated melt pools, with a repetition rate of 10 Hz and a
212 fluence of ~15 J/cm^2. Following each analysis, a 1-minute washout period brought the system back
213 to its background state. All ablations occurred in a helium (He) atmosphere before entering into
214 the plasma torch. Background counts were measured for 10 s prior to each ablation followed by
215 ~40 s ablation signal. Measurements were performed with the ICP-MS using the medium mass
216 resolution mode (m/Δm = 3000). Two to three scans were conducted in each of the glass, whereas
217 only one scan was conducted in each sulfide grain. Data were collected for the following masses:
218 ^{59}Co, ^{60}Ni, ^{95}Mo, ^{101}Ru, ^{105}Pd, ^{185}Re, ^{190}Os and ^{195}Pt. Analyses of unknowns were accompanied by
219 the analysis of SRM NIST 610 and NIST 612 before and after the sample acquisition, which
220 provided the calibration curves for determining element concentrations and for constraining
221 instrument drift. Data were processed using in house data reduction software, which determines
222 element concentrations based on ratios of count rates for samples and standards, known
223 concentrations in the standards, and the known concentration of an internal standard element in
224 the unknowns. Detection limits for each spot or line analysis can differ considerably from element
225 to element depending on background, count rate, and laser ablation parameters. In all cases data
226 are reported for signals that are distinguishable at 3 standard deviation above background. For
227 additional details on the LA-ICP-MS technique, please refer to Lee et al. (2008).
228
229 **3. RESULTS**
230 Figure 1 shows the back-scattered electron (BSE) images of some of the experiments from
231 this study. Table 2 reports the phase assemblages, major element compositions of carbonated melts

along with the *P-T* conditions of the experiments, estimated fO_2 of the experiments and measured SCSS values. Supplementary Table S1 reports the major element composition of the sulfide melts of this study. Table 3 reports the HSE and chalcophile elements concentration in sulfide and carbonated melt, and Table 4 reports the partition coefficients of these elements between sulfide and carbonated melt ($D^{\text{sulfide/carb. melt}}$).

3.1. Experimental textures

Two immiscible melt phases: a quenched carbonated melt and a quenched sulfide melt (Fig. 1) are present in all experiments. We speculate that equilibrium silicate phases were present in some of the experiments as such phases have been observed in previous experiments at similar *P-T* and with similar bulk compositions (Chowdhury and Dasgupta, 2020). We are unable to determine the identity of those phases because of our experimental design and the chosen sample preparation approach as discussed in section 2.2. The texture of the carbonated melts is mostly composed of dendritic crystals which include carbonates, silicates, and sub-micron sulfide droplets. We assume that these sub-micron sulfide droplets formed during rapid cooling of the melts and represent original sulfur that was dissolved in the carbonated silicate melt at experimental temperatures. The small size of the quenched phases in the melt pools gave us the ability to obtain an average composition of the melt with a defocused beam of 20-40 μm using EPMA and 25-80 μm using LA-ICP-MS. As the grain size of these quenched phases started to increase near the vicinity of large sulfide globules, where they found a substrate to grow larger crystals on, we chose to keep our melt analyses away from those to yield more accurate results. Fig 1b shows a sulfide blob and quenched carbonated silicate melt with LA-ICP-MS pits.

3.2. Assessment of chemical equilibrium

To assess an approach to equilibrium we can use several lines of evidence. (a) Sulfur content in the carbonated silicate melts doesn't show any discernible variability across the experimental sample volume. (b) Although diffusivity for sulfur in carbonated melts are not known to our knowledge, the diffusivity of S^{2-} in basaltic melt at sulfide saturation is known (Freda et al., 2005). Applying those S^{2-} diffusivity in our experimental conditions, we get values of 1×10^{-11} m^2/s to 1.5×10^{-10} m^2/s, which when applied to our experimental durations show diffusion length for S to be 1000-1050 μm. The farthest edge of the container from the sulfide blobs are around 200- 500 μm, which indicates that the entire volume of the experimental sample is expected to be equilibrated within the experimental duration. Given diffusivity of most chemical species in carbonated melts are faster than in more viscous silicate melts, equilibration within our experimental duration is not expected to be an issue. (c) Comparing SCSS measured in the experiments of the current study with the model of Chowdhury and Dasgupta (2020), we see less than 5% deviation from the 1:1 line (Supplementary Fig. 1) indicating equilibrium has been achieved in the experiments of this study.

3.3. Carbonated melt compositions, HSE and chalcophile element concentrations in sulfide and melt

The difference in composition of the experimental melts from the starting mixes is attributed to crystallization of silicates to a varying degree. For CSL1 and CSL2, SiO_2 contents are 27-32 wt.% and 14-17 wt.%, respectively and Al_2O_3 varies from 2.5 to 5 wt.% and 0.2 to 1.6 wt.%, respectively. For experiments with these two starting compositions, FeO* contents are 9.5-12 wt.% and 7-10 wt.%, MgO contents are 17-26 wt.% and 25-32 wt.%, whereas CaO varies from 25 to 32

wt.% and 31 to 44 wt.%, respectively. CO_2 content was estimated by the difference of 100 wt.% and EPMA analytical total (following Lane and Dalton, 1994). It varies from 20 to 22 wt.% for CSL1and from 33 to 40 wt.% for CSL2. Measured SCSS for these melts are 0.18-0.31 wt.% for CSL1 and 0.08-0.2 wt.% for CSL2.

Similar to Chowdhury and Dasgupta (2020), we used the equilibrium presence of carbonated melts in graphite capsule to determine the experimental oxygen fugacity, fO_2 following the calibration of Stagno and Frost (2010). Table 2 lists the calculated logfO_2 of the experimental assemblages, which vary between ΔFMQ of ~-1.88 to ~-2.38.

The HSE and chalcophile element concentrations in the carbonated and sulfide melts are reported in Table 3. The $D^{\text{sulfide/carb. melt}}$ for HSEs and chalcophile elements are calculated by ratio of the concentration of these elements in sulfide melt and in carbonated melt (Table 4, Fig. 2). Comparison of $D^{\text{sulfide/carb. melt}}$ of HSEs (Os, Ru, Pt, Pd and Re) for melt with low CO_2 (CSL1) and high CO_2 (CSL2) shows that $D^{\text{sulfide/carb. melt}}$ values are higher in the system where the melt CO_2 content is lower (more silica rich), whereas, for chalcophile elements (Co, Ni and Mo) the behavior is opposite (i.e. $D^{\text{sulfide/carb. melt}}$ values are lower in the system where the melt CO_2 content is lower). The $D^{\text{sulfide/carb. melt}}$ values do not show any significant variation as a function of temperature.

4. DISCUSSION

4.1. Comparison of $D^{\text{sulfide/carbonated melt}}$ with previously constrained $D^{\text{sulfide/silicate melt}}$

The partition coefficients of HSE and chalcophile elements between sulfide liquid and carbonated melts determined by *in situ* analysis in this study are compared with previous studies, which have determined partition coefficients of these elements between sulfide melt and basaltic silicate melt (Fig. 3). Past measurements for HSEs included both bulk analytical methods to

301 determine the metal content of glass and sulfide (Peach et al., 1990; Fleet et al., 1996; Crocket et
302 al., 1997; Roy-Barman et al., 1998) as well as in situ LA-ICP-MS analyses (Mungall and Brenan,
303 2014). For other chalcophile elements (Co, Ni and Mo), measurements were done by *in situ* LA-
304 ICP-MS (Li and Audétat, 2012; Kiseeva and Wood, 2013). All the PGEs measured in this study
305 (Os, Ru, Pt and Pd) have $D^{\text{sulfide/carb. melt}}$ values lower than $D^{\text{sulfide/silicate melt}}$ values measured by
306 Mungall and Brenan (2014), whereas HSE (Re) and the chalcophile elements (Co, Ni and Mo)
307 have *D* values higher than what was measured in previous studies (Li and Audétat, 2012; Kiseeva
308 and Wood, 2013; Mungall and Brenan, 2014). $D^{\text{sulfide/carb. melt}}$ for both the systems investigated in
309 this study (CSL1 and CSL2) show similar trends and the sequence is Mo < Co < Ni < Re < Pt ≤
310 Pd < Ru ≤ Os. Between the two starting compositions, the one with higher CO_2 (CSL2) has lower
311 $D^{\text{sulfide/carb. melt}}$ values, indicating *D* values of HSEs decrease with increasing CO_2 content in the
312 melt. These difference in *D* values mean that the PGEs are more easily extractable via carbonated
313 silicate melt compared to silicate (basaltic) melt, whereas other HSE (Re) and chalcophile elements
314 behave oppositely. Carbonatitic and carbonated silicate melt can, hence, mobilize more PGEs as
315 compared to basaltic melts, which might result in higher PGE content in primary carbonatitic, and
316 kimberlitic melts compared to those in basalts.
317
318 **4.2. Bulk partition coefficients applicable to carbonated melt generation from partial melting**
319 **of peridotite**
320 In this section we estimate bulk partition coefficients relevant for carbonatite and
321 kimberlite generation at deep upper mantle conditions (Table 5, Fig. 4). A bulk partition coefficient
322 ($\overline{D}$) for an element is calculated for the residue/carbonated silicate melt system as a linear
323 combination of the proportions of sulfide melt and silicate minerals multiplied by their respective

D's. The silicate residue is considered to be represented by a garnet lherzolite (61% olivine, 18% clinopyroxene, 5% orthopyroxene and 16% garnet), a dunite (100% olivine) and a wehrlite (75% olivine and 25% clinopyroxene). The peridotitic mantle is assumed to be sulfide saturated with bulk sulfur content of 250 ppm (McDonough and Sun, 1995). The $D^{ol/melt}$ for HSEs are taken from Brenan et al. (2003), $D^{cpx/melt}$ for Ru, Pt and Re are from Hill et al. (2000), Righter et al. (2002) and Dasgupta et al. (2009), and $D^{opx/melt}$ for Re is from Righter et al. (2002). $D^{gt/melt}$ for Re was taken from Dasgupta et al. (2009). Where data are unavailable, we assumed mineral-melt partitioning based on similarity in ionic sizes (for cpx/melt), lesser compatibility of elements in orthopyroxene compared to clinopyroxene (e.g., less than $D^{cpx/melt}$ by a factor of 10 for $D^{opx/melt}$) and a constant value of 0.39 for $D^{gt/melt}$ [similar to $D^{gt/melt}$ for Re from Dasgupta et al. (2009)].

Although several HSEs are compatible in spinel, D values are much lower in chromite than in magnetite, lessening the effect on $\overline{D}$. Also, low fO_2 significantly reduces HSE incorporation in spinel (Brenan et al., 2012) and very low modal abundances compared to olivine make spinel an unlikely candidate to play a major role in HSE distribution between residue and carbonated melt at fO_2 conditions prevalent for carbonated peridotite melting at subcontinental lithospheric mantle and oceanic mantle.

Compared to bulk partition coefficients for sulfide-bearing peridotite and silicate melt systems (Mungall and Brenan, 2014), the bulk partition coefficients for sulfide-bearing peridotite and carbonated melt systems are lower for PGEs (Os, Ru, Pt and Pd) but higher for Re for systems with both higher- and lower-CO_2 carbonated melts as shown in Fig. 4. The increased affinity of the PGEs toward carbonated melt during mantle melting is chiefly due to the lower $D^{sulfide/carb.\ melt}$ of these elements compared to $D^{sulfide/silicate\ melt}$. The I-PGEs (Ru and Os) show greater affinity towards carbonated melt compared to the P-PGEs (Pt and Pd), but the extent of incompatibility is

higher in the systems with lower CO_2 content bearing melt. Calculating bulk *D* for a garnet lherzolite, a dunite and a wehrlite residue shows very little difference because the presence of a sulfide phase exerts primary control on the distribution of PGEs and HSEs in the mantle.

To calculate HSE concentrations of low degree mantle derived melts of carbonated peridotites, HSEs are distributed between the carbonated silicate melt and residue (sulfide-bearing garnet lherzolite, dunite, and wehrlite) using $\overline{D}$ and the aggregate fractional melting model:

$$\frac{C_L}{C_0} = \frac{1}{F} \times [1 - (1 - F)^{1/\overline{D}}] \quad (1)$$

where C_L is the concentration of an HSE in the carbonated melt derived from the melting of carbonated mantle peridotite, C_0 is the initial concentration of the HSE in the mantle (PM) taken from McDonough and Sun (1995), $\overline{D}$ is the bulk *D* calculated for the sulfide-bearing residue and carbonated melt system and *F* is the degree of melting. Fig. 5 shows the plot of HSEs normalized by their primitive mantle values based on this aggregate fractional melting model for a low CO_2 kimberlitic melt and a high CO_2 carbonatitic melt. The plot shows that P-PGEs (Pt and Pd) and Re are more enriched in the primary carbonatitic and kimberlitic melt than I-PGEs (Os and Ru) or conversely, I-PGEs are retained in the sulfide-bearing mantle residue preferentially compared to the P-PGEs and Re, after carbonated melt extraction.

4.3. The dependence of $\overline{D}$ and HSE content of carbonated melt on S content of the mantle source

In the last section we established that the HSE content of carbonated melt is primarily controlled by presence or absence of sulfide in the residue. To evaluate how the initial sulfur content in the mantle affects the HSE distribution during mantle melting, we calculated - using the aggregate fractional melting equation (Eqn. 1) - the HSE content of the carbonated melt for S content in the mantle varying between 5 and 300 ppm, encompassing the primitive mantle (PM) S

content of 250 ppm (McDonough and Sun, 1995) and covering the full range of estimated S content of the Earth's mantle (e.g., Saal et al., 2002; Salters and Stracke, 2004; Ding and Dasgupta, 2017). The $\overline{D}$ for the mantle residue-carbonated melt system in the presence of sulfide changes with varying S content. In Fig. 6, we plot the HSE content of the carbonated melt normalized to PM with varying S content in the mantle source. With decreasing bulk S content in the mantle source, HSE mobilization via carbonated melt increases for both kimberlitic and carbonatitic melt compositions by as much as 2 orders of magnitude, but the extent of mobilization is greater via carbonatitic melt owing to lower $D^{\text{sulfide/carb. melt}}$ values.

4.4. Comparison of the modelled HSE contents of primary carbonated melts with the HSE contents of natural carbonatites and kimberlites

Many studies have previously measured PGE and HSE contents of natural carbonatites and kimberlites (Xu et al., 2008; Maier et al., 2017; Ackerman et al., 2019; He et al., 2020, Tappe et al., 2020). Maier et al. (2017) documented the PGE systematics of kimberlites from Karelian, Finland and Kaapvaal, South Africa to be characterized by two components, (i) a peridotitic detritus of sub-continental lithospheric mantle (SCLM) with high I-PGE/P-PGE ratio and (ii) a melt with low I-PGE/P-PGE ratio, similar to what we expect from our melting model for the carbonated melt and the peridotitic residue. PGE systematics of carbonatites from China (Xu et al., 2008), Kaapvaal, South Africa (Tappe et al., 2020), and Tamil Nadu, India (Ackerman et al., 2019) show trends of low I-PGE/P-PGE ratio similar to primitive carbonatitic melt from our aggregate fractional melting model, but the concentrations of PGEs are an order of magnitude lower than those calculated from our model even with S content as high as 300 ppm in the primitive mantle. The low PGE abundance of natural carbonatites can be due to significant modification of

parental carbonatitic melts at Tamil Nadu, India by interaction with ambient crustal materials and post-magmatic hydrothermal alteration (Ackerman et al., 2019) and can also be affected by complex evolution history of carbonatites after their first formation in the mantle. Moreover, magnetite, which can deplete PGEs further, has been documented during late evolution of Tamil Nadu carbonatites (Capobianco et al., 1994). He et al. (2020) showed that carbonatites from Dalihu, North China have significantly higher PGE contents compared to previous PGE measurements in carbonatites (Xu et al., 2008; Ackerman et al., 2019). These authors (He et al., 2020) attributed the higher PGE contents of their studied carbonatites to derivation from a mantle domain where sulfide was transformed to sulfate owing to reactive implantation of sedimentary carbonates as an oxidizing agent. In Fig. 7, we plot PM normalized concentration of HSEs (PGEs and Re) from natural carbonatites, kimberlites, along with natural ocean-island basalts (OIBs) and alkali basalts. We also plot HSE contents calculated using bulk D estimated using our experimental $D^{\text{sulfide/carb. melt}}$ and aggregate fractional melting model for a S content in the primitive mantle varying from 5 to 300 ppm. The OIB and alkali basalt HSE contents are taken from studies by Day et al. (2010) and Day (2013), respectively, whereas carbonatites and kimberlites' HSE contents are taken from the aforementioned studies. In Fig. 7a, we plot the HSE contents according to bulk Ds calculated for lower CO_2 kimberlitic melt compositions. The alkali basalt HSE pattern can be described by our aggregate fractional melting model for a sulfide saturated PM with 100-300 ppm S. The Canadian shield, Premier, and Karelian kimberlites might need components from SCLM peridotites to describe their HSE patterns as they differ from the calculated primary kimberlitic melt pattern. This feature of kimberlites are also acknowledged in some previous studies (Tappe et al., 2017; Maier et al., 2017). In Fig. 7b, we plot the HSE contents according to bulk Ds calculated for high-CO_2 content carbonatitic melt compositions. It also shows that the HSE pattern

of OIBs is very similar to a carbonatitic melt derived from a sulfide saturated PM with 100 ppm S. The Dalihu carbonatites can be described using our aggregate fractional melting model with 100-300 ppm S in the PM for different PGEs. The Tamil Nadu, India carbonatites are very low in HSE concentrations and cannot be reproduced by our aggregate fractional melting model HSE pattern, which might be because of the fractionation of magnetite, which incorporate HSEs in the late stage of evolution of a carbonatite (Ackerman et al., 2019). Another reason which can explain the deviation of HSE pattern of carbonatites from our modelled liquid HSE pattern is that some of the natural carbonatite bodies are not true liquid but rather are rich in cumulus phases. Hence, we should not expect such natural carbonatite compositions to be identical to the HSE pattern of a model carbonated peridotite melt.

4.5. Re-Os systematics of carbonated silicate melts

^{187}Os with 1.5% isotopic abundance is a product of radioactive decay of ^{187}Re ($\lambda = 1.666 \times 10^{-11}$ year^{-1}) (Carlson, 2005). The partitioning behavior of HSEs (Fig. 4), and observations in most mafic-ultramafic systems, show that partial melting of the mantle will produce a melt with high Re/Os ratio, whereas the melt depleted peridotite residue will have low Re/Os ratio. Previous studies have presented variations in $^{187}Os/^{188}Os$ in kimberlites, lamproites, and carbonatite (Lambert et al., 1995; Araujo et al., 2001; Ackerman et al., 2019; Tappe et al., 2020). The variations in $^{187}Os/^{188}Os$ in these rocks was mainly attributed to lowering of oxygen fugacity in the source of these rocks during metasomatism, leading to destabilization of Os-Ir-Ru alloys and allowing a large proportions of Os to enter the melt (Andrews and Brenan, 2002). Other possible explanation discussed in previous studies include assimilation of substantial quantities of mantle xenoliths in these rocks (Carlson and Nowell, 2001; Le Roex et al., 2003) and mobilization of Os

in fluids associated with mantle metasomatism (Carlson, 2005). These variabilities can also be related to heterogeneity in the source regions.

However, based on the determined $D^{\text{sulfide/carb. melt}}$ from this study and comparing with $D^{\text{sulfide/silicate melt}}$ (Mungall and Brenan, 2014), we also expect a different extent of Re-Os fractionation for carbonated melt-bearing systems versus silicate melt-bearing systems. In particular: (i) carbonated melts generated from a sulfide-bearing mantle will have lower Re/Os ratio than the silicate melts generated from a similarly sulfide-bearing mantle. (ii) a sulfide-bearing peridotite residue from which a carbonated melt is extracted will have higher Re/Os ratio than a sulfide-bearing peridotite residue from which a silicate melt is extracted. Both these features are expected because $\left|D_{Os}^{sulfide/carb.\ melt} < D_{Os}^{sulfide/silicate}\right.$ and $\left|D_{Re}^{sulfide/carb.\ melt} > D_{Re}^{sulfide/silicate}\right.$.

The $^{187}Os/^{188}Os$ of carbonated melts i.e., the $^{187}Os/^{188}Os$ ratio of parental kimberlites and carbonatites will evolve to higher values than the melt depleted peridotites but will be lower than basaltic silicate melts because $\left|D_{Os}^{sulfide/carb.\ melt} < D_{Os}^{sulfide/silicate}\right.$ and $\left|D_{Re}^{sulfide/carb.\ melt} > D_{Re}^{sulfide/silicate}\right.$, which leads to higher $^{187}Re/^{188}Os$ in mantle-derived basaltic melts than carbonated mantle melts. Using $^{187}Re/^{188}Os$ ratio of a primary carbonated melt calculated based on our estimated bulk D and the aggregate fractional melting equation, the proportion of carbonate melt which metasomatizes the sub-lithospheric mantle peridotite xenoliths can be calculated if $(^{187}Os/^{188}Os)_{initial}$ and timing of the metasomatic event is known. We calculated γOs and Re/Os of peridotite residue after carbonatitic partial melt extraction and a silicate partial melt extraction at various times (3 Ga, 2 Ga and 1 Ga) in the past, from a sulfide-bearing mantle. We used our calculated bulk D for the garnet lherzolite-carbonated melt equilibration and $D^{\text{sulfide/silicate}}$ from Mungall and Brenan (2014) for the bulk D calculation and used that bulk D for

garnet lherzolite-silicate melt equilibration. Fig. 8 shows a simple mixing between a carbonated melt and silicate melt extracted at 0.5 Ga calculated using $(^{187}Os/^{188}Os)_{initial} = 0.1215$ (Walker et al., 1989) for a primitive mantle with various peridotite residues in a γOs vs Re/Os plot. We also plot Kaapvaal craton and Siberia peridotites (Pearson et al., 1995) to see whether a single stage melt extraction and carbonated melt or silicate melt addition can explain the γOs and Re-Os systematics observed in the peridotites. Some of the Kaapvaal craton and Siberia peridotite xenoliths show that they can be explained by silicate or carbonate melt extraction. Some of the peridotites, however, require two-component mixing between depleted mantle residue and low degree carbonated melt, whereas a few other xenoliths can be explained by mixing between depleted mantle residue and silicate melt. Our calculations presented in Figure 8 show that to explain the spread in Re/Os ratio observed in Siberian and Kaapvaal peridotitic mantle xenoliths, carbonate melt metasomatism would require a greater proportion of melt implantation (~4-8 wt.%), whereas similar effects can be obtained by much lower extent of basaltic melt implantation (~0.1-0.3 wt.%). Thus, Re/Os systematics of a depleted peridotite will be less prone to modification with episodes of metasomatic enrichment caused by carbonated melt as opposed to similar metasomatic enrichment by basaltic melt.

4.6. Estimating proportion of peridotite detritus in natural kimberlites and carbonatites

Kimberlites are characterized by high abundances of incompatible trace elements (e.g., Th, Ba, Rb, LREE, Sr etc.) as well as of compatible elements like Mg and Ni. The abundances of both compatible and incompatible elements are thought to be a reflection of mixing between primary kimberlitic melt (rich in incompatible elements) and lithospheric mantle peridotite (MgO- and Ni-rich) xenoliths (Kjarsgaard et al., 2009). The evidence of mixing is reflected in binary Ir vs Ru or

Ir vs MgO plots and are well documented in Maier et al. (2017) for Karelian and Kaapvaal kimberlites. Previous studies have aimed at quantifying the proportion of peridotite detritus and kimberlitic melt using various different modelling approaches like mixing model of Os isotope ratios (Pearson et al., 2003; Tappe et al., 2017) and Nd-Hf isotopes (Tappe et al., 2013). Some studies have tried to calculate the primary kimberlitic melt composition from the composition of non-xenocrystic olivine (Arndt et al., 2010), analysis of quenched kimberlitic melt (Price et al., 2000; Kopylova et al., 2007) and by mass balance using Ir contents (Maier et al., 2017). In Fig. 9 we compare the PM normalized HSE pattern of a primary kimberlitic melt calculated by Maier et al. (2017) and the pattern modelled using bulk *D*s and aggregate fractional melting equation in this study. The difference in all the HSE concentrations and the pattern in general between our calculations and that reported in Maier et al. (2017) in Fig. 9 calls for modelling the natural kimberlite composition as a product of mixing between the detritus SCLM peridotite and a true kimberlitic melt.

Here we estimate the proportion of detrital material and the composition of the detrital material in natural kimberlite from Karelian, Kaapvaal and Canadian shield craton using mass balance of Ru contents in a method similar to mass balance by Ir content discussed in Maier et al. (2017). Ru behaves similarly to Ir both being part of I-PGEs. Their abundances in low degree carbonatitic and kimberlitic melts are very different from lithospheric peridotites. Also, Ru is chosen for practical reasons; as our experiments lacked doped Ir, we couldn't measure *D* values for Ir between carbonated melt and sulfide melt.

The following mass balance equations apply:

$$[C_i(km) \times f(km)] + [C_i(d) \times f(d)] = Ci(sample) \quad (2)$$

505 where C_i(km) is the concentration of an HSE in the primary kimberlitic melt calculated using our
506 bulk *D* and aggregate fractional melting equation, f(km) is the fraction of the primary kimberlitic
507 melt, C_i(d) is the concentration of HSE in the detritus SCLM peridotite and f(d) is the fraction of
508 the detritus. Here, f(d) = 1- f(km) (3)
509 Arranging accordingly from equation (2), we get,
510 $C_i(d) = \{C_i(sample) - [C_i(km) \times f(km)]\} / [1 - f(km)]$ (4)
511 To get the fraction of peridotite detritus we need to find the fraction of kimberlitic melt first and
512 then equate for f(d) using equation (3).
513 $f(km) = [C_i(sample) - C_i(d)] / [C_i(km) - C_i(d)]$ (5)
514 To solve equation (5) using Ru as the element for mass balance, C_{Ru}(d) is taken from previous
515 studies that have measured Ru concentration in the mantle xenoliths of Karelian, Kaapvaal and
516 Canadian Shield craton recovered from kimberlite pipe (Irvine et al., 2003; Maier et al., 2012) and
517 C_{Ru}(km) is taken from our aggregate fractional melting model for bulk *D*s calculated for low-CO_2
518 kimberlitic melt for an extent of melting of 0.3 wt.%.
519 The compositions of mantle xenoliths are shown to be very homogenous for Karelian and
520 Kaapvaal craton (Maier et al., 2017) at 6.33 ppb Ru for Karelian xenoliths, 5.98 ppb for Kaapvaal
521 xenoliths and 6.69 for Canadian shield craton (Irvine et al.,2003). Calculations using equation (5)
522 followed by equation (3), suggest that the fraction of detritus lithospheric mantle peridotites
523 contribute ~2-28% of the material in Group I and II kimberlites from Finland. For the two Premier
524 samples, the contribution from detritus is 25-40%. For Canadian shield craton samples, the
525 contribution is 6-17%. These estimates overlap with Maier et al. (2017) for these samples (3-22%
526 for Finland; 19-28% for Premier) and Tappe et al. (2017) for Canadian kimberlites (2-30%).
527 Calculating the model detritus xenolith from equation (4) we see that all other HSEs fall within

528 the range of measured peridotite xenoliths from Karelian, Kaapvaal and Canadian shield craton
529 (Fig. 10).

530 For carbonatites from Dalihu, China we calculated proportion of mantle xenolith detritus
531 using equation (5) and (3). The C_{Ru}(d) is taken from previous studies that have measured Ru
532 concentration in the mantle xenoliths from North China Craton (Zhang et al., 2008; Liu et al.,
533 2010) and C_{Ru}(carb. melt) is taken from our aggregate fractional melting model for bulk *D*s
534 calculated for high CO_2 carbonatitic melt representing 0.01% melting degree. Calculation suggests
535 that the proportion of detritus from North China Craton (NCC) in the Dalihu carbonatites is
536 between 6-35 %. One sample with higher Ru content shows 52% assimilation of detritus. Fig. 11
537 shows calculation of other HSEs based on our mass balance model using Ru concentration yield a
538 model detritus xenolith composition, which lies within the natural NCC peridotites.

539 The mass balance calculation using Ru concentrations can therefore be used as an
540 additional method to look into natural kimberlite and carbonatitic compositions and determine the
541 volume of peridotite detritus as an assimilant. This method shows good correlation with methods
542 previously used to determine detritus volume using Os isotopic composition (Tappe et al., 2017),
543 Nd-Hf isotopes (Tappe et al., 2013), and mass balance using Ir contents (Maier et al., 2017). Thus,
544 our experimentally measured *D* values of HSEs between carbonated melt and sulfide melt can be
545 used to calculate the bulk *D*s and furthermore applied in melting models to calculate HSE
546 concentrations for primary carbonated melt and investigate natural carbonated melt samples to
547 understand HSE and PGE systematics of kimberlites and carbonatites in cratonic lithospheric
548 mantle.

549 *4.7. Association of carbonated magmas and PGE deposits*

The variable proportions of mantle detritus necessary to explain the geochemistry of kimberlites from places like Kaapvaal, Karelian, and Canadian shield suggest that HSEs are indeed scavenged by the low degree carbonated and kimberlitic melts. This carbonated melt-SCLM interactions could be responsible of high Os contents of Large Igneous Provinces (LIPs), which eventually leads to formation of large PGE deposits such as that seen in Kaapvaal craton (Zhang et al., 2008). Beneath cratons, plume induced melting, which eventually results in the formation of LIPs also causes generation of kimberlitic melt from previously metasomatized, carbonated lithospheric mantle (Sun and Dasgupta, 2020). Kimberlitic melts formed through melting of deeper, SCLM domains can percolate to thinner parts of the continental mantle where melting is more focused and variable degrees of interactions between the melt and SCLM result in formation of Ni-Cu-PGE deposits (Griffin et al., 2013). The presence of carbonated melts mainly enhances the availability of PGEs to form economically important deposits because *D* values of PGEs between sulfide and carbonated melts are lower than *D* values of PGEs between sulfide and silicate melts, resulting in higher concentrations of PGEs in processes involving carbonated melt-lithosphere interactions rather than basaltic melt-lithosphere interactions.

5. CONCLUSION

Our experimentally determined partition coefficients of HSEs (Os, Ru, Pt, Pd and Re) and chalcophile elements (Co, Ni and Mo) between sulfide melt and carbonated melt suggest that these elements are very compatible in sulfide melt with *D* values of Mo being on the order of 10^1, Co on the order of 10^2, Ni on the order of 10^3, Pt, Pd, and Re on the order of 10^4 and Ru and Os on the order of 10^5 for melts with low CO_2 (kimberlitic). For more CO_2-rich carbonatitic compositions, *D* values of Mo are on the order of 10^1, Co on the order of 10^2, Ni and Re on the

573 order of 10^3 and Os, Ru, Pt and Pd are in the order of 10^4. Comparison with previous studies on
574 sulfide-silicate melt system reveals that the *D* values for sulfide melt-carbonated melt systems are
575 lower, making HSEs more mobile in carbonated melts than in silicate melts (basalts). Among
576 carbonated melt-bearing systems, the sulfide-melt *D*s are lower for carbonatitic melt- compared to
577 kimberlitic melt-bearing systems. We calculated bulk *D* values assuming a garnet lherzolite, a
578 dunite, and a wehrlite residue after melt extraction from a carbonated peridotite and calculated
579 HSE concentrations in the low degree (0.1-1 wt.%) kimberlitic and carbonatitic melts using an
580 aggregate fractional melting equation. Comparing primitive mantle normalized HSE patterns from
581 our calculations with natural kimberlites and carbonatites show that some carbonatite patterns
582 (from Tamil Nadu, India, and China) match with low degree melt patterns but the concentrations
583 are much lower and need fractionation of magnetite to describe their HSE contents. Other
584 carbonatites (Dalihu) can be described by derivation from a lower S content primitive mantle or
585 can be explained by the presence of lithospheric mantle xenolith detritus. Kimberlites from
586 Karelian, Finland; Kaapvaal, South Africa, and Canadian shield Craton, Canada shows evidence
587 of presence of mantle xenolith detritus. Using Ru concentrations and mass balance calculation, we
588 show that the proportion of these xenolith detritus is 2-28% for Karelian, Finland, 25-40% for
589 Kaapvaal, South Africa, and 6-16% for the Canadian shield, all of which overlap with modelled
590 calculations shown by previous studies using various other proxies. Modelling similarly for Dalihu
591 carbonatites, we obtain 6-35 % xenolith detritus in the carbonatites. HSE systematics, thus, suggest
592 the contribution of both low-degree primary carbonated mantle melt and assimilated lithospheric
593 mantle peridotite in explaining the HSE geochemistry of natural kimberlites and carbonatites.
594 Comparison of our estimated D_{Re}/D_{Os} for sulfide-bearing peridotite-carbonated melt systems with
595 the same ratio for sulfide-bearing peridotite-basaltic melt systems suggest lesser fractionation of

Re/Os during extraction of carbonated melt. Hence with similar extent of melt metasomatism, peridotite domains would show lesser extent of resetting in Re/Os systematics if the agent of metasomatism is a carbonatitic melt as opposed to a basaltic melt.

ACKNOWLEDGMENT

PC wants to thank Gelu Costin for his help during EPMA analysis. RD acknowledges NSF EAR-1763226 grant and PC acknowledges Geological Society of America graduate student research grant for this study. We thank Dr. Sebastian Tappe and two anonymous reviewers for their constructive reviews, which helped us improve our communication. We also thank Bernard Charlier for efficient handling of the manuscript as an associate editor.

REFERENCES

Ackerman L., Polák L., Magna T., Rapprich V., Ďurišová J. and Upadhyay D. (2019) Highly siderophile element geochemistry and Re–Os isotopic systematics of carbonatites: Insights from Tamil Nadu, India. *Earth Planet. Sci. Lett.* **520**, 175–187.

Adam J. and Green T. (2006) Trace element partitioning between mica- and amphibole-bearing garnet lherzolite and hydrous basanitic melt: 1. Experimental results and the investigation of controls on partitioning behaviour. *Contrib. to Mineral. Petrol.* **152**, 1–17.

Alard O., Lorand J.-P., Reisberg L., Bodinier J.-L., Dautria J.-M. and O'Reilly S. Y. (2011) Volatile-rich Metasomatism in Montferrier Xenoliths (Southern France): Implications for the Abundances of Chalcophile and Highly Siderophile Elements in the Subcontinental Mantle. *J. Petrol.* **52**, 2009–2045.

Alt J. C., Shanks W. C. and Jackson M. C. (1993) Cycling of sulfur in subduction zones: The

geochemistry of sulfur in the Mariana Island Arc and back-arc trough. *Earth Planet. Sci. Lett.* **119**, 477–494.

Andrews D. R. A. and Brenan J. M. (2002) *The solubility of ruthenium in sulfide liquid: implications for platinum group mineral stability and sulfide melt-silicate melt partitioning*.,

Araujo A., Carlson R. W., Gaspar J. C. and Bizzi L. A. (2001) Petrology of kamafugites and kimberlites from the Alto Paranaíba Alkaline Province, Minas Gerais, Brazil. *Contrib. to Mineral. Petrol.* **142**, 163–177.

Arndt N. T., Guitreau M., Boullier A.-M., Le Roex A., Tommasi A., Cordier P. and Sobolev A. (2010) Olivine, and the Origin of Kimberlite. *J. Petrol.* **51**, 573–602.

Aulbach S., Luchs T. and Brey G. P. (2014) Distribution and behaviour during metasomatism of PGE–Re and Os isotopes in off-craton mantle xenoliths from Namibia. *Lithos* **184**–**187**, 478–490.

Barnes S. J., Naldrett A. J. and Gorton M. P. (1985) The origin of the fractionation of platinum-group elements in terrestrial magmas. *Chem. Geol.* **53**, 303–323.

Bézos A., Lorand J. P., Humler E. and Gros M. (2005) Platinum-group element systematics in Mid-Oceanic Ridge basaltic glasses from the Pacific, Atlantic, and Indian Oceans. *Geochim. Cosmochim. Acta* **69**, 2613–2627.

Le Bras L. Y., Bolhar R., Bybee G. M., Nex P. A. M., Guy B. M., Moyana T. and Lourens P. (2020) Platinum-group and trace elements in Cu-sulfides from the Loolekop pipe, Phalaborwa: implications for ore-forming processes. *Miner. Depos.* **56**, 161–177.

Brenan J. M. (2008) The Platinum-Group Elements: “Admirably Adapted” for Science and Industry. *Elements* **4**, 227–232.

Brenan J. M., Finnigan C. F., McDonough W. F. and Homolova V. (2012) Experimental

642 constraints on the partitioning of Ru, Rh, Ir, Pt and Pd between chromite and silicate melt:
643 The importance of ferric iron. *Chem. Geol.* **302**–**303**, 16–32.
644 Brenan J. M., McDonough W. F. and Dalpé C. (2003) Experimental constraints on the
645 partitioning of rhenium and some platinum-group elements between olivine and silicate
646 melt. *Earth Planet. Sci. Lett.* **212**, 135–150.
647 Brounce M., Stolper E. and Eiler J. (2017) Redox variations in Mauna Kea lavas, the oxygen
648 fugacity of the Hawaiian plume, and the role of volcanic gases in Earth's oxygenation.
649 *Proc. Natl. Acad. Sci. U. S. A.* **114**, 8997–9002.
650 Buono A. S., Dasgupta R., Lee C. T. A. and Walker D. (2013) Siderophile element partitioning
651 between cohenite and liquid in the Fe-Ni-S-C system and implications for geochemistry of
652 planetary cores and mantles. *Geochim. Cosmochim. Acta* **120**, 239–250.
653 Buono A. S. and Walker D. (2011) The Fe-rich liquidus in the Fe–FeS system from 1 bar to
654 10 GPa. *Geochim. Cosmochim. Acta* **75**, 2072–2087.
655 Burness S., Smart K. A., Tappe S., Stevens G., Woodland A. B. and Cano E. (2020) Sulphur-rich
656 mantle metasomatism of Kaapvaal craton eclogites and its role in redox-controlled platinum
657 group element mobility. *Chem. Geol.* **542**.
658 Campbell A. J. and Humayun M. (2005) Compositions of group IVB iron meteorites and their
659 parent melt. *Geochim. Cosmochim. Acta* **69**, 4733–4744.
660 Canil D. and Fellows S. A. (2017) Sulphide–sulphate stability and melting in subducted sediment
661 and its role in arc mantle redox and chalcophile cycling in space and time. *Earth Planet.*
662 *Sci. Lett.* **470**, 73–86.
663 Capobianco C. J., Hervig R. L. and Drake M. J. (1994) Experiments on crystal/liquid partitioning
664 of Ru, Rh and Pd for magnetite and hematite solid solutions crystallized from silicate melt.

665 *Chem. Geol.* **113**, 23–43.
666 Carlson R. W. (2005) Application of the Pt-Re-Os isotopic systems to mantle geochemistry and
667 geochronology. *Lithos* **82**, 249–272.
668 Carlson R. W. and Nowell G. M. (2001) of the Colorado Plateau. *Geochemistry Geophys.*
669 *Geosystems* **2**.
670 Chowdhury P. and Dasgupta R. (2019) Effect of sulfate on the basaltic liquidus and Sulfur
671 Concentration at Anhydrite Saturation (SCAS) of hydrous basalts – Implications for sulfur
672 cycle in subduction zones. *Chem. Geol.* **522**, 162–174.
673 Chowdhury P. and Dasgupta R. (2020) Sulfur extraction via carbonated melts from sulfide-
674 bearing mantle lithologies – Implications for deep sulfur cycle and mantle redox. *Geochim.*
675 *Cosmochim. Acta* **269**, 376–397.
676 Crocket J. H., Fleet M. E. and Stone W. E. (1997) Implications of composition for experimental
677 partitioning of platinum-group elements and gold between sulfide liquid and basalt melt:
678 The significance of nickel content. *Geochim. Cosmochim. Acta* **61**, 4139–4149.
679 Dasgupta R. (2018) Volatile-bearing partial melts beneath oceans and continents–Where, how
680 much, and of what compositions? *Am. J. Sci.* **318**, 141–165.
681 Dasgupta R. and Hirschmann M. M. (2010) The deep carbon cycle and melting in Earth's
682 interior. *Earth Planet. Sci. Lett.* **298**, 1–13.
683 Dasgupta R., Hirschmann M. M., McDonough W. F., Spiegelman M. and Withers A. C. (2009)
684 Trace element partitioning between garnet lherzolite and carbonatite at 6.6 and 8.6 GPa
685 with applications to the geochemistry of the mantle and of mantle-derived melts. *Chem.*
686 *Geol.* **262**, 57–77.
687 Dasgupta R., Hirschmann M. M. and Smith N. D. (2007a) Partial Melting Experiments of

688 Peridotite + CO2 at 3 GPa and Genesis of Alkalic Ocean Island Basalts. *J. Petrol.* **48**,
689 2093–2124.
690 Dasgupta R., Hirschmann M. M. and Smith N. D. (2007b) Water follows carbon: CO 2 incites
691 deep silicate melting and dehydration beneath mid-ocean ridges. *Geology* **35**, 135–138.
692 Dasgupta R., Mallik A., Tsuno K., Withers A. C., Hirth G. and Hirschmann M. M. (2013)
693 Carbon-dioxide-rich silicate melt in the Earth's upper mantle. *Nature* **493**, 211–215.
694 Day J. M. D. (2013) Hotspot volcanism and highly siderophile elements. *Chem. Geol.* **341**, 50–
695 74.
696 Day J. M. D., Pearson D. G., Macpherson C. G., Lowry D. and Carracedo J. C. (2010) Evidence
697 for distinct proportions of subducted oceanic crust and lithosphere in HIMU-type mantle
698 beneath El Hierro and La Palma, Canary Islands. *Geochim. Cosmochim. Acta* **74**, 6565–
699 6589.
700 Ding S. and Dasgupta R. (2018) Sulfur inventory of ocean island basalt source regions
701 constrained by modeling the fate of sulfide during decompression melting of a
702 heterogeneous mantle. *J. Petrol.* **59**, 1281–1308.
703 Ding S. and Dasgupta R. (2017) The fate of sulfide during decompression melting of peridotite –
704 implications for sulfur inventory of the MORB-source depleted upper mantle. *Earth Planet.*
705 *Sci. Lett.* **459**, 183–195.
706 Dunn T. and Sen C. (1994) Mineral/matrix partition coefficients for orthopyroxene, plagioclase,
707 and olivine in basaltic to andesitic systems: A combined analytical and experimental study.
708 *Geochim. Cosmochim. Acta* **58**, 717–733.
709 Fleet M. E., Crocket J. H. and Stone W. E. (1996) Partitioning of platinum-group elements (Os,
710 Ir, Ru, Pt, Pd) and gold between sulfide liquid and basalt melt. *Geochim. Cosmochim. Acta*

60, 2397–2412.

Fonseca R. O. C., Campbell I. H., O'Neill H. S. C. and Allen C. M. (2009) Solubility of Pt in sulphide mattes: Implications for the genesis of PGE-rich horizons in layered intrusions. *Geochim. Cosmochim. Acta* **73**, 5764–5777.

Fontana J. (2006) Phoscorite-Carbonatite Pipe Complexes. *Platin. Met. Rev.* **50**, 134–142.

Freda C., Baker D. R. and Scarlato P. (2005) Sulfur diffusion in basaltic melts. *Geochim. Cosmochim. Acta* **69**, 5061–5069.

Frost D. J. and McCammon C. A. (2008) The Redox State of Earth's Mantle. *Annu. Rev. Earth Planet. Sci.* **36**, 389–420.

Gannoun A., Burton K. W., Day J. M. D., Harvey J., Schiano P. and Parkinson I. (2015) Highly siderophile element and Os isotope systematics of volcanic rocks at divergent and convergent plate boundaries and in intraplate settings. *Rev. Mineral. Geochemistry* **81**, 651–724.

Griffin W. L., Begg G. C. and O'Reilly S. Y. (2013) Continental-root control on the genesis of magmatic ore deposits. *Nat. Geosci.* **6**, 905–910.

Harvey J., Warren J. M. and Shirey S. B. (2016) Mantle Sulfides and their Role in Re–Os and Pb Isotope Geochronology. *Rev. Mineral. Geochemistry* **81**, 579–649.

He D., Liu Y., Moynier F., Foley S. F. and Chen C. (2020) Platinum group element mobilization in the mantle enhanced by recycled sedimentary carbonate. *Earth Planet. Sci. Lett.* **541**, 116262.

Hill E., Wood B. J. and Blundy J. D. (2000) The effect of Ca-Tschermaks component on trace element partitioning between clinopyroxene and silicate melt. *Lithos* **53**, 203–215.

Irvine G. J., Pearson D. G., Kjarsgaard B. A., Carlson R. W., Kopylova M. G. and Dreibus G.

(2003) A Re–Os isotope and PGE study of kimberlite-derived peridotite xenoliths from Somerset Island and a comparison to the Slave and Kaapvaal cratons. *Lithos* **71**, 461–488.

Jégo S. and Dasgupta R. (2013) Fluid-present melting of sulfide-bearing ocean-crust: Experimental constraints on the transport of sulfur from subducting slab to mantle wedge. *Geochim. Cosmochim. Acta* **110**, 106–134.

Jégo S. and Dasgupta R. (2014) The Fate of Sulfur During Fluid-Present Melting of Subducting Basaltic Crust at Variable Oxygen Fugacity. *J. Petrol.* **55**, 1019–1050.

Jorgenson C. (2017) Sulphur solubility of carbonatites as a mass transfer agent in the mantle. .

Kelemen P. B., Yogodzinski G. M. and Scholl D. W. (2003) Along-strike variation in the Aleutian Island Arc: Genesis of high Mg# andesite and implications for continental crust. In *Geophysical Monograph Series* Blackwell Publishing Ltd. pp. 223–276.

Keller T., Katz R. F. and Hirschmann M. M. (2017) Volatiles beneath mid-ocean ridges: Deep melting, channelised transport, focusing, and metasomatism. *Earth Planet. Sci. Lett.* **464**, 55–68.

Kiseeva E. S. and Wood B. J. (2013) A simple model for chalcophile element partitioning between sulphide and silicate liquids with geochemical applications. *Earth Planet. Sci. Lett.* **383**, 68–81.

Kopylova M. G., Matveev S. and Raudsepp M. (2007) Searching for parental kimberlite melt. *Geochim. Cosmochim. Acta* **71**, 3616–3629.

Lambert D. D., Shirey S. B. and Bergman S. C. (1995) Proterozoic lithospheric mantle source for the Prairie Creek lamproites: Re-Os and Sm-Nd isotopic evidence. *Geology* **23**, 273–276.

Lane S. J. and Dalton J. A. (1994) *Electron microprobe analysis of geological carbonates*.,

Lee C.-T. A., Oka M., Luffi P. and Agranier A. (2008) Internal distribution of Li and B in

757 serpentinites from the Feather River Ophiolite, California, based on laser ablation
758 inductively coupled plasma mass spectrometry. *Geochemistry, Geophys. Geosystems* **9**, n/a-
759 n/a.
760 Li J.-L., Schwarzenbach E. M., John T., Ague J. J., Huang F., Gao J., Klemd R., Whitehouse M.
761 J. and Wang X.-S. (2020) Uncovering and quantifying the subduction zone sulfur cycle
762 from the slab perspective. *Nat. Commun.* **11**, 514.
763 Li Y. and Audétat A. (2012) Partitioning of V, Mn, Co, Ni, Cu, Zn, As, Mo, Ag, Sn, Sb, W, Au,
764 Pb, and Bi between sulfide phases and hydrous basanite melt at upper mantle conditions.
765 *Earth Planet. Sci. Lett.* **355**–**356**, 327–340.
766 Liu J., Rudnick R. L., Walker R. J., Gao S., Wu F. and Piccoli P. M. (2010) Processes
767 controlling highly siderophile element fractionations in xenolithic peridotites and their
768 influence on Os isotopes. *Earth Planet. Sci. Lett.* **297**, 287–297.
769 Lorand J. P., Delpech G., Grégoire M., Moine B., O'Reilly S. Y. and Cottin J. Y. (2004)
770 Platinum-group elements and the multistage metasomatic history of Kerguelen lithospheric
771 mantle (South Indian Ocean). In *Chemical Geology* Elsevier B.V. pp. 195–215.
772 Lorand J. P., Luguet A. and Alard O. (2013) Platinum-group element systematics and
773 petrogenetic processing of the continental upper mantle: A review. *Lithos* **164**–**167**, 2–21.
774 Maier W. D., O'Brien H., Peltonen P. and Barnes S. J. (2017) Platinum-group element contents
775 of Karelian kimberlites: Implications for the PGE budget of the sub-continental lithospheric
776 mantle. *Geochim. Cosmochim. Acta* **216**, 358–371.
777 Maier W. D., Peltonen P., McDonald I., Barnes S. J., Barnes S.-J., Hatton C. and Viljoen F.
778 (2012) The concentration of platinum-group elements and gold in southern African and
779 Karelian kimberlite-hosted mantle xenoliths: Implications for the noble metal content of the

Earth's mantle. *Chem. Geol.* **302**–**303**, 119–135.

McDonough W. F. and Sun S. -s. (1995) The composition of the Earth. *Chem. Geol.* **120**, 223–253.

Mondal S. K. (2011) Platinum group element (PGE) geochemistry to understand the chemical evolution of the Earth's mantle. *J. Geol. Soc. India* **77**, 295–302.

Moussallam Y., Longpré M.-A., McCammon C., Gomez-Ulla A., Rose-Koga E. F., Scaillet B., Peters N., Gennaro E., Paris R. and Oppenheimer C. (2019) Mantle plumes are oxidised. *Earth Planet. Sci. Lett.* **527**, 115798.

Moussallam Y., Morizet Y., Massuyeau M., Laumonier M. and Gaillard F. (2015) CO 2 solubility in kimberlite melts. *Chem. Geol.* **418**, 198–205.

Mungall J. and Brenan J. (2014) Partitioning of platinum-group elements and Au between sulfide liquid and basalt and the origins of mantle-crust fractionation of the chalcophile elements. *Geochim. Cosmochim. Acta* **125**, 265–289.

Mungall J. E. and Brenan J. M. (2014) Partitioning of platinum-group elements and Au between sulfide liquid and basalt and the origins of mantle-crust fractionation of the chalcophile elements. *Geochim. Cosmochim. Acta* **125**, 265–289.

Patten C., Barnes S.-J., Mathez E. A. and Jenner F. E. (2013) Partition coefficients of chalcophile elements between sulfide and silicate melts and the early crystallization history of sulfide liquid: LA-ICP-MS analysis of MORB sulfide droplets. *Chem. Geol.* **358**, 170–188.

Peach C. ., Mathez E. . and Keays R. . (1990) Sulfide melt-silicate melt distribution coefficients for noble metals and other chalcophile elements as deduced from MORB: Implications for partial melting. *Geochim. Cosmochim. Acta* **54**, 3379–3389.

Pearson D. ., Canil D. and Shirey S. . (2003) Mantle Samples Included in Volcanic Rocks:

803 Xenoliths and Diamonds. In *Treatise on Geochemistry* Elsevier. pp. 171–275.
804 Pearson D. G., Shirey S. B., Carlson R. W., Boyd F. R., Pokhilenko N. P. and Shimizu N. (1995)
805 ReOs, SmNd, and RbSr isotope evidence for thick Archaean lithospheric mantle beneath the
806 Siberian craton modified by multistage metasomatism. *Geochim. Cosmochim. Acta* **59**,
807 959–977.
808 Poli S. (2015) Carbon mobilized at shallow depths in subduction zones by carbonatitic liquids.
809 *Nat. Geosci.* **8**, 633–636.
810 Price S. E., Russell J. K. and Kopylova M. G. (2000) Primitive Magma From the Jericho Pipe,
811 N.W.T., Canada: Constraints on Primary Kimberlite Melt Chemistry. *J. Petrol.* **41**, 789–
812 808.
813 Pruseth K. L. and Palme H. (2004) The solubility of Pt in liquid Fe-sulfides. In *Chemical*
814 *Geology* Elsevier B.V. pp. 233–245.
815 Puchtel I. S. and Humayun M. (2001) Platinum group element fractionation in a komatiitic basalt
816 lava lake. *Geochim. Cosmochim. Acta* **65**, 2979–2993.
817 Rehkämper M., Halliday A. N., Fitton J. G., Lee D.-C., Wieneke M. and Arndt N. T. (1999) Ir,
818 Ru, Pt, and Pd in basalts and komatiites: new constraints for the geochemical behavior of
819 the platinum-group elements in the mantle. *Geochim. Cosmochim. Acta* **63**, 3915–3934.
820 Righter K., Campbell A. J., Humayun M. and Hervig R. L. (2004) Partitioning of Ru, Rh, Pd,
821 Re, Ir, and Au between Cr-bearing spinel, olivine, pyroxene and silicate melts. *Geochim.*
822 *Cosmochim. Acta* **68**, 867–880.
823 Le Roex A. P., Bell D. R. and Davis P. (2003) Petrogenesis of group I Kimberlites from
824 Kimberley, South Africa: Evidence from bulk-rock geochemistry. *J. Petrol.* **44**, 2261–2286.
825 Roy-Barman M., Wasserburg G. J., Papanastassiou D. A. and Chaussidon M. (1998) Osmium

826 isotopic compositions and Re-Os concentrations in sulfide globules from basaltic glasses.
827 *Earth Planet. Sci. Lett.* **154**, 331–347.
828 Saal A. E., Hauri E. H., Langmuir C. H. and Perfit M. R. (2002) Vapour undersaturation in
829 primitive mid-ocean-ridge basalt and the volatile content of earth's upper mantle. *Nature*
830 **419**, 451–455.
831 Salters V. J. M. and Stracke A. (2004) Composition of the depleted mantle. *Geochemistry,*
832 *Geophys. Geosystems* **5**, n/a-n/a.
833 Stagno V. and Frost D. J. (2010) Carbon speciation in the asthenosphere: Experimental
834 measurements of the redox conditions at which carbonate-bearing melts coexist with
835 graphite or diamond in peridotite assemblages. *Earth Planet. Sci. Lett.* **300**, 72–84.
836 Stagno V., Ojwang D. O., McCammon C. A. and Frost D. J. (2013) The oxidation state of the
837 mantle and the extraction of carbon from Earth's interior. *Nature* **493**, 84–88.
838 Sun C. and Dasgupta R. (2019) Slab–mantle interaction, carbon transport, and kimberlite
839 generation in the deep upper mantle. *Earth Planet. Sci. Lett.* **506**, 38–52.
840 Sun C. and Dasgupta R. (2020) Thermobarometry of CO_2-rich, silica-undersaturated melts
841 constrains cratonic lithosphere thinning through time in areas of kimberlitic magmatism.
842 *Earth Planet. Sci. Lett.* **550**, 116549.
843 Tappe S., Brand N. B., Stracke A., van Acken D., Liu C. Z., Strauss H., Wu F. Y., Luguet A. and
844 Mitchell R. H. (2017) Plates or plumes in the origin of kimberlites: U/Pb perovskite and Sr-
845 Nd-Hf-Os-C-O isotope constraints from the Superior craton (Canada). *Chem. Geol.* **455**,
846 57–83.
847 Tappe S., Graham Pearson D., Kjarsgaard B. A., Nowell G. and Dowall D. (2013) Mantle
848 transition zone input to kimberlite magmatism near a subduction zone: Origin of anomalous

Nd-Hf isotope systematics at Lac de Gras, Canada. *Earth Planet. Sci. Lett.* **371**–**372**, 235–251.

Tappe S., Stracke A., van Acken D., Strauss H. and Luguet A. (2020) Origins of kimberlites and carbonatites during continental collision – Insights beyond decoupled Nd-Hf isotopes. *Earth-Science Rev.* **208**, 103287.

Tomkins A. G. and Evans K. A. (2015) Separate zones of sulfate and sulfide release from subducted mafic oceanic crust. *Earth Planet. Sci. Lett.* **428**, 73–83.

Tsuno K. and Dasgupta R. (2015) Fe–Ni–Cu–C–S phase relations at high pressures and temperatures – The role of sulfur in carbon storage and diamond stability at mid- to deep-upper mantle. *Earth Planet. Sci. Lett.* **412**, 132–142.

Tsuno K. and Dasgupta R. (2011) Melting phase relation of nominally anhydrous, carbonated pelitic-eclogite at 2.5-3.0 GPa and deep cycling of sedimentary carbon. *Contrib. to Mineral. Petrol.* **161**, 743–763.

Walker R. J., Carlson R. W., Shirey S. B. and F.R B. (1989) Os, Sr, Nd, and Pb isotope systematics of southern African peridotite xenoliths: Implications for the chemical evolution of subcontinental mantle. *Geochim. Cosmochim. Acta* **53**, 1583–1595.

Wallace P. J. and Edmonds M. (2011) The Sulfur Budget in Magmas: Evidence from Melt Inclusions, Submarine Glasses, and Volcanic Gas Emissions. *Rev. Mineral. Geochemistry* **73**, 215–246.

Walters J. B., Cruz-Uribe A. M. and Marschall H. R. (2020) Sulfur loss from subducted altered oceanic crust and implications for mantle oxidation. *Geochem. Persp. Let* **13**, 36–41.

Xu C., Qi L., Huang Z., Chen Y., Yu X., Wang L. and Li E. (2008) Abundances and significance of platinum group elements in carbonatites from China. *Lithos* **105**, 201–207.

872 Zhang H. F., Goldstein S. L., Zhou X. H., Sun M., Zheng J. P. and Cai Y. (2008) Evolution of
873 subcontinental lithospheric mantle beneath eastern China: Re-Os isotopic evidence from
874 mantle xenoliths in Paleozoic kimberlites and Mesozoic basalts. *Contrib. to Mineral. Petrol.*
875 **155**, 271–293.
876 Zhang M., O'Reilly S. Y., Wang K.-L., Hronsky J. and Griffin W. L. (2008) Flood basalts and
877 metallogeny: The lithospheric mantle connection. *Earth-Science Rev.* **86**, 145–174.
878

Table 1: Starting compositions used in this study.

	CSL1	CSL2
SiO2	29.87	15.25
TiO2	1.33	0.70
Al2O3	4.98	0.51
FeO	9.96	4.81
MnO	0.25	0.14
MgO	19.08	26.16
CaO	16.59	18.11
Na2O	0.91	2.35
K2O	0.03	0.32
CO2	17.01	31.64
Total	100.00	100.00

	Sulfide
Fe	63.53
S	36.47

*starting compositions are from Chowdhury and Dasgupta (2020)

Table 2: Experimental run conditions, oxygen fugacity and major element composition of experimental quenched melts (in wt.%) measured using EPMA.

Run No.	*P* (GPa)	*T* (°C)	fO_2 (ΔFMQ)	Phase asseblages^	time (hours)	*n*[c]	SiO_2	TiO_2	Al_2O_3	FeO*	MnO	MgO	CaO	K_2O	Na_2O	S	Total[a]	CO_2[b]
B476a[$]	3	1600	-2.06	qm+sb	2	18	28.44	1.87	3.59	9.68	0.74	26.62	27.14	0.07	1.54	0.31	100	20.38
1σ							1.43	0.26	0.71	0.92	0.06	1.24	1.05	0.01	0.37	0.06		
B476b[#]	3	1600	-2.05	qm+sb	2	14	17.22	1.47	1.66	10.44	0.68	32.17	31.68	0.38	4.1	0.2	100	33.68
1σ							1.17	0.47	0.25	0.97	0.08	1.47	1.31	0.04	0.82	0.07		
G631a[$]	3	1500	-2.15	qm+sb	15	15	32.14	1.87	2.66	10.25	0.54	25.64	25.24	0.04	1.34	0.28	100	22.14
1σ							1.88	0.47	0.88	1.14	0.03	1.06	0.97	0.01	0.21	0.04		
G631b[#]	3	1500	-2.38	qm+sb	15	12	15.27	1.14	1.18	11.22	0.87	31.44	34.21	0.57	3.88	0.22	100	34.77
1σ							0.84	0.21	0.39	0.85	0.06	1.38	1.14	0.11	1.07	0.04		
G633a[$]	3	1300	-2.11	qm+sb	24	9	27.29	2.49	5.26	12.37	0.75	17.45	32.49	0.11	1.61	0.18	100	22.76
1σ							0.83	0.12	0.25	0.35	0.04	1.01	0.45	0.03	0.41	0.04		
G633b[#]	3	1300	-1.88	qm+sb	24	13	14.83	0.99	0.18	6.93	0.86	25.92	44.74	0.31	5.16	0.08	100	40.38
1σ							0.58	0.11	0.04	0.44	0.02	0.83	1.26	0.03	0.72	0.001		

*FeO total

[a]Total and the major element oxide concentrations of the melts are reported on a CO_2-free basis.

[b]CO_2 based on difference of EPMA analytical sum from 100 wt.%

[c]*n* = number of EPMA spot analyses used to obtain the average melt compositions

^All the experiments had observable qm: quenched carbonated silicate matrix and sb: sulfide blobs. Because we cut the containers transversely, to obtain polished surfaces of two bulk compositions at once, we could not document possibly equilibrium minerals that are present at the cooler end (bottom) of the capsule chambers. Comparing our experimental conditions with those of Chowdhury and Dasgupta (2020) who conducted sulfide solubility and phase relations using the same melt compositions, we have insights on the expected mineral assemblage that can be present at the cooler end of capsule chambers for the following experiments – G631a: olivine + orthopyroxene + clinopyroxene; G633a: olivine + orthopyroxene + garnet, whereas B476a is expected to be super-liquidus. For other experimental samples, similar comparison could not be made, as complete phase assemblage information was also not available in Chowdhury and Dasgupta (2020) given the focus of that study was sulfur solubility at sulfide saturation for carbonated melts.

[$]These experiments used CSL1 as the starting mix.

[#]These experiments used CSL2 as the staring mix.

909 **Table 3:** Mean values of HSE and chalcophile elements in quenched melt and sulfide melt measured using LA-ICP-MS (in ppm).

910

CSL 1 (Kimberlitic)					CSL 2 (Carbonatitic)				
B476a	Sulfide Melt	1σ	Carbonated Melt	1σ	B476b	Sulfide Melt	1σ	Carbonated Melt	1σ
	n=2		n=4			n=3		n=3	
Co	4065	158	7.96	1.12	Co	3331	202	6.96	0.87
Ni	4101	274	1.20	0.47	Ni	3350	189	0.9	0.22
Mo	568	98	58.40	5.42	Mo	1476	87	18.68	1.91
Ru	979	102	0.01	0.002	Ru	2181	136	0.04	0.01
Pd	1401	122	0.06	0.004	Pd	815	98	0.05	0.02
Re	5175	274	2.30	0.16	Re	985	75	0.5	0.05
Os	2007	136	0.01	0.002	Os	2107	147	0.04	0.006
Pt	3856	265	0.24	0.08	Pt	2800	212	0.15	0.02
G631a	Sulfide Melt	1σ	Carbonated Melt	1σ	G631b	Sulfide Melt	1σ	Carbonated Melt	1σ
	n=1*		n=3			n=2		n=4	
Co	3411	-	11.04	1.35	Co	4206	309	9.1	0.91
Ni	4175	-	2.04	0.38	Ni	3781	236	1.2	0.34
Mo	647	-	83.84	6.87	Mo	1500	128	18.83	1.06
Ru	2237	-	0.02	0.001	Ru	1897	189	0.03	0.006
Pd	1684	-	0.05	0.003	Pd	983	133	0.06	0.01
Re	5303	-	2.39	0.47	Re	524	92	0.4	0.12
Os	3147	-	0.02	0.001	Os	2287	274	0.05	0.008
Pt	4178	-	0.17	0.08	Pt	3241	341	0.17	0.07
G633a	Sulfide Melt	1σ	Carbonated Melt	1σ	G633b	Sulfide Melt	1σ	Carbonated Melt	1σ
	n=2		n=3			n=2		n=5	
Co	4113	213	11.9	0.97	Co	3148	281	8.4	1.32
Ni	4098	183	1.38	0.21	Ni	2540	227	0.7	0.14
Mo	522	97	71.17	3.47	Mo	1355	125	15.77	1.66
Ru	1020	126	0.01	0.002	Ru	1964	179	0.05	0.004
Pd	1064	113	0.04	0.003	Pd	656	104	0.04	0.007
Re	6905	269	2.8	0.14	Re	534	117	0.3	0.01
Os	2104	194	0.02	0.001	Os	2371	273	0.03	0.002
Pt	2276	165	0.13	0.05	Pt	3893	320	0.22	0.04

911

912 * 1σ based on replicate analyses. As only one sulfide analysis was done, we don't report 1σ for G631a.

913 **Table 4:** Sulfide melt- carbonated silicate melt partition coefficients

	CSL 1 (Kimberlitic)		CSL 2 (Carbonatitic)	
	$D^{\text{sulfide/carb.melt}}$	1σ	$D^{\text{sulfide/carb.melt}}$	1σ
Co	388	24	439	64
Ni	2811	104	3500	122
Mo	8	0.47	82	3.54
Ru	103906	2541	52349	987
Pd	27876	874	16354	414
Re	2455	135	1686	176
Os	154380	3458	59155	1024
Pt	19382	697	18475	865

914

915 T**able 5:** Calculated bulk *D*s applicable for peridotite-derived carbonated melts (carbonatite and kimberlite) under upper mantle melting conditions.

916

Low CO_2 (Kimberlitic) Melt					Mass fractions	Gt- Lherzolite	Dunite	Wehrlite
Olivine						0.61	0.99975	0.749
Cpx						0.18	0	0.249
Opx						0.05	0	0
Garnet						0.16	0	0
Sulfide						0.00025	0.00025	0.00025
	$D^{Ol/carb.\ melt}$	$D^{Cpx/carb.\ melt}$	$D^{Opx/carb.\ melt}$	$D^{Gt/carb.\ melt}$	$D^{sulfide/carb.\ melt}$	Bulk *D*	Bulk *D*	Bulk *D*
Co	2[a]	0.95[g]	2[a]	1.78[g]	388	1.87	2.10	1.83
Ni	10[a]	3[a]	4[a]	5[a]	2811	8.34	10.70	8.94
Mo	0.11[c]	0.016[d]	0.0039[d]	0.003[d]	8	0.07	0.11	0.09
Ru	1.6	1[e]	*0.5*	*0.39*	103906	27.22	27.58	27.42
Pd	0.021	*0.12*	*0.01*	*0.39*	27878	7.07	6.99	7.02
Re	0.001	0.18[f]	0.013[f]	0.39[g]	2455	0.71	0.61	0.66
Os	0.001	*0.18*	*0.013*	*0.39*	154380	38.69	38.60	38.64
Pt	0.009	1.5[f]	*0.15*	*0.39*	19382	5.19	4.85	5.23
High CO_2 (Carbonatitic) Melt					Mass fractions	Gt- Lherzolite	Dunite	Wehrlite
Olivine						0.61	0.99975	0.749
Cpx						0.18	0	0.249
Opx						0.05	0	0
Garnet						0.16	0	0
Sulfide						0.00025	0.00025	0.00025
	$D^{Ol/carb.\ melt}$	$D^{Cpx/carb.\ melt}$	$D^{Opx/carb.\ melt}$	$D^{Gt/carb.\ melt}$	$D^{sulfide/carb.\ melt}$	Bulk *D*	Bulk *D*	Bulk *D*
Co	2[a]	0.95[g]	2[a]	1.78[g]	439	1.89	2.11	1.84
Ni	10[a]	3[a]	4[a]	5[a]	3500	8.52	10.87	9.11
Mo	0.11[c]	0.016[d]	0.0039[d]	0.003[d]	82	0.09	0.13	0.11
Ru	1.6	1e	*0.5*	*0.39*	52340	14.33	14.68	14.53
Pd	0.021	*0.12*	*0.01*	*0.39*	16354	4.19	4.11	4.13
Re	0.001	0.18$_f$	0.013[f]	0.39[g]	1686	0.52	0.42	0.47
Os	0.001	*0.18*	*0.013*	*0.39*	59155	14.88	14.79	14.83
Pt	0.009	1.5[f]	*0.15*	*0.39*	18475	4.96	4.63	5.00

917

918 [a]from Kelemen et al. (2003); [c]from Dunn and Sen (1994); [d]from Adam and Green, (2006); [e]from Hill et al. (2000); [f]from Righter et al. (2004); [g]from Dasgupta et al. (2009); underlined data are from Brenan et al.,

919 (2003) and the numbers in italics are assumed.

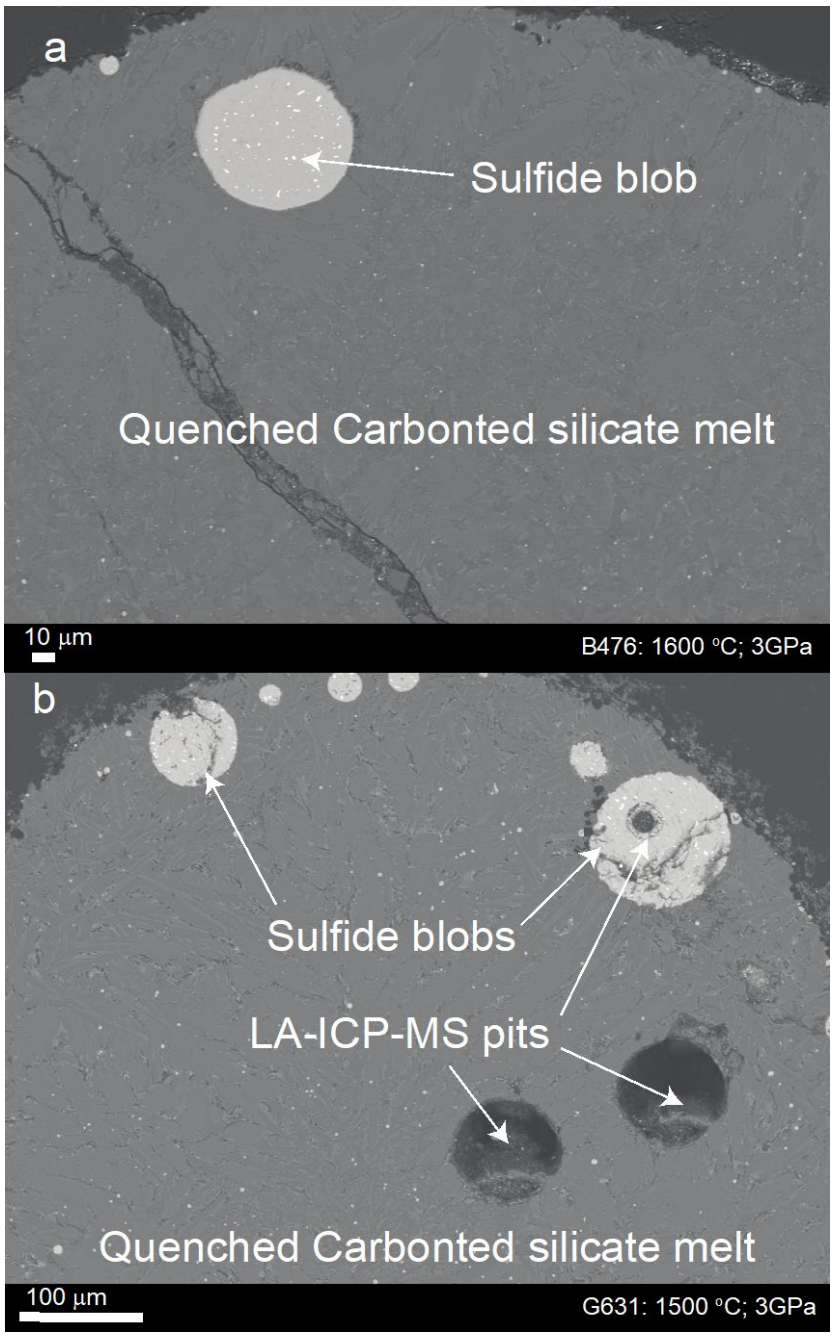

Figure 1: Phase assemblage and texture of the experiments: (a) A part of the capsule showing the sulfide blobs and the quenched melt. The quenched melts and sulfide melt blobs were analyzed with a 20-40 µm beam in EPMA. (b) Quenched melt and sulfide melt blobs along with LA-ICP-MS pits.

926 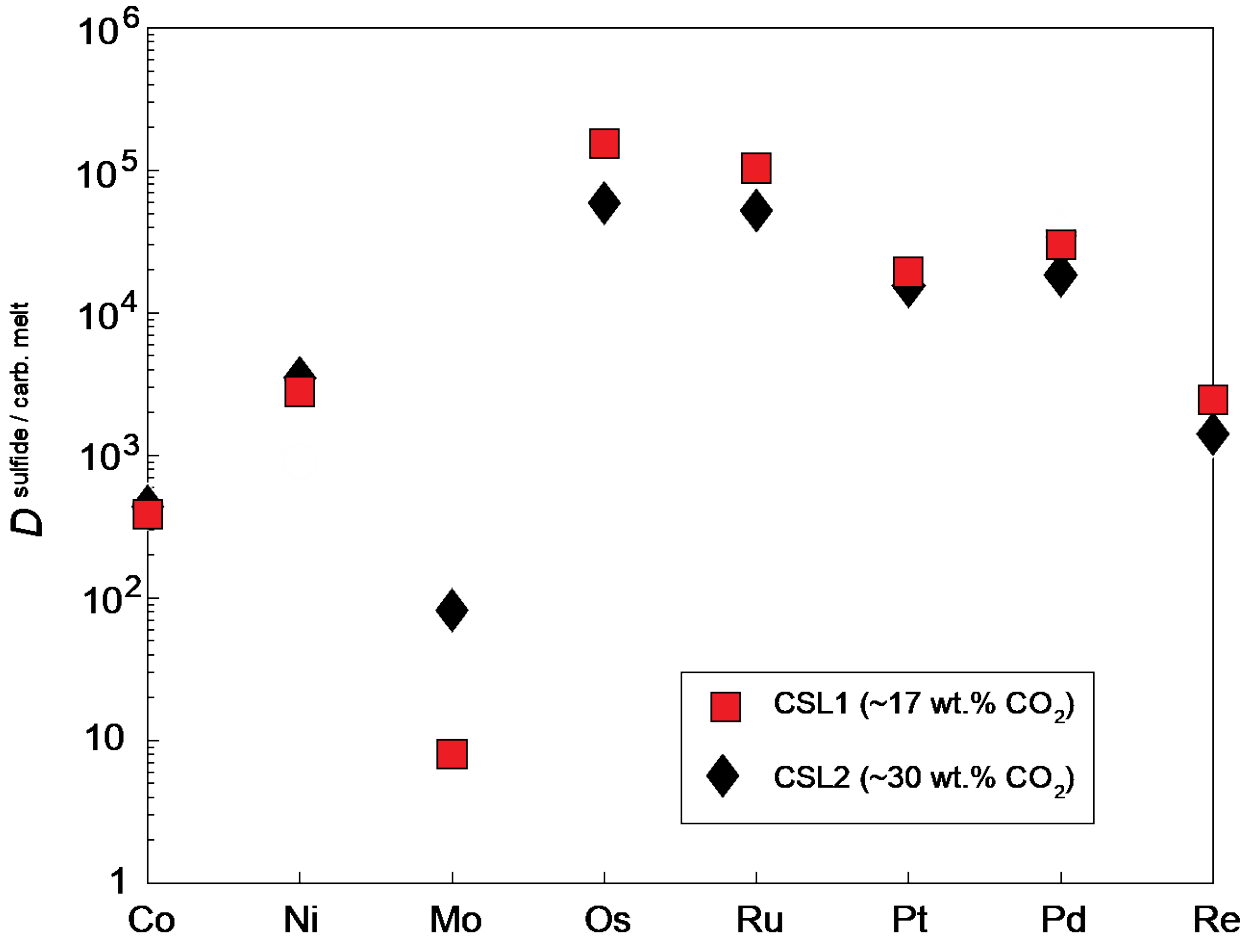

927 **Figure 2**: Partition coefficients of chalcophile (Co, Ni, Mo) and Highly-Siderophile Elements (Os,
928 Ru, Pt, Pd, Re) between sulfide melt and carbonated melt ($D^{\text{sulfide/carb. melt}}$) for low-$CO_2$ (CSL1) and
929 high CO_2 (CSL2) melt, reported from Table 3.

930

931 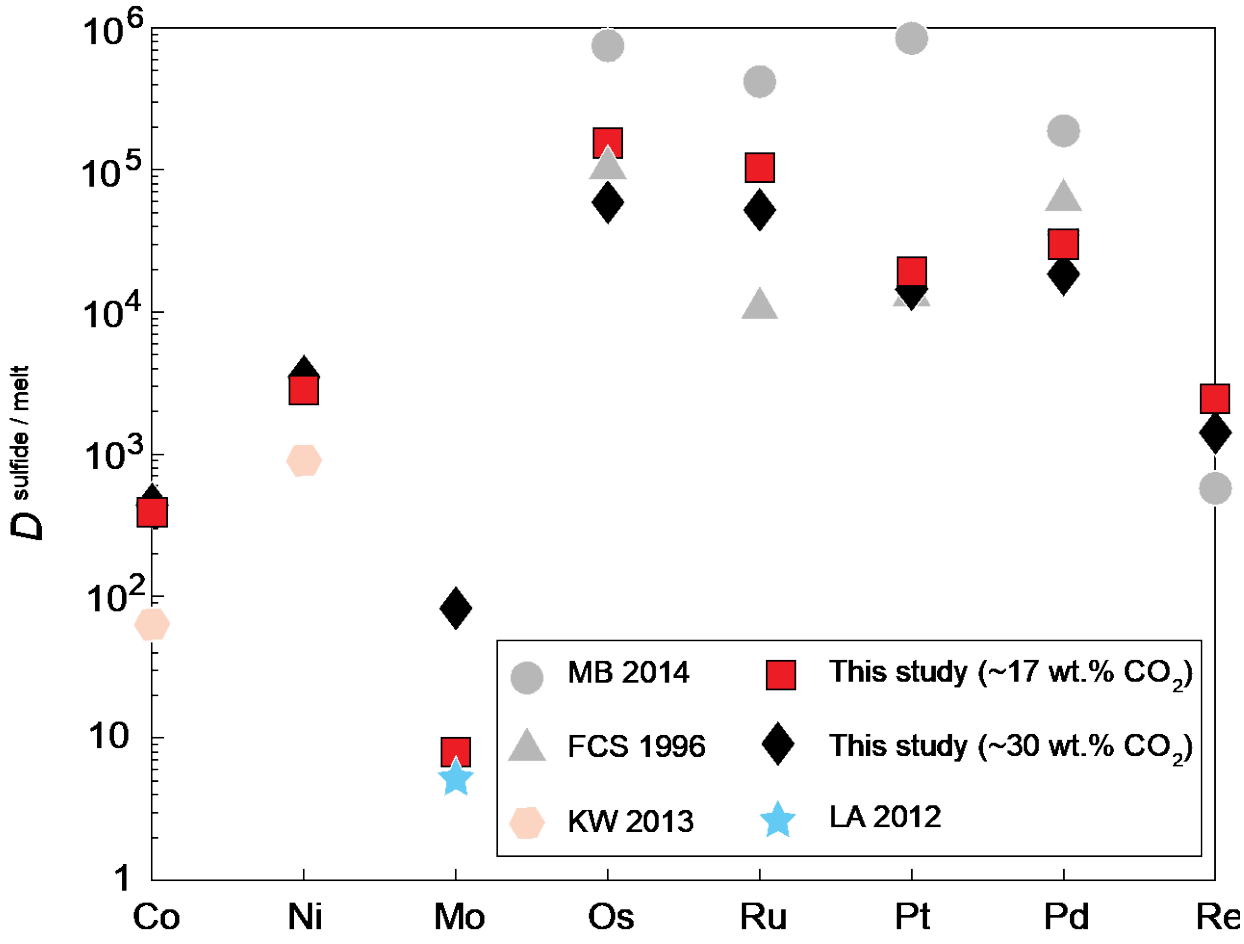

932 **Figure 3**: Partition coefficients of chalcophile (Co, Ni, Mo) and Highly-Siderophile Elements (Os,
933 Ru, Pt, Pd, Re) between sulfide melt and carbonated melt ($D^{\text{sulfide/carb. melt}}$) for low CO_2 (CSL1) and
934 high CO_2 (CSL2) melt. Plotted for comparison are the $D^{\text{sulfide/silicate melt}}$ from previous experiments
935 for comparison. MB 2014 - Mungall and Brenan (2014); FCS 1996 - Fleet et al. (1996); KW 2013
936 - Kiseeva and Wood (2013) and LA 2012 - Li and Audétat (2012).

937

938

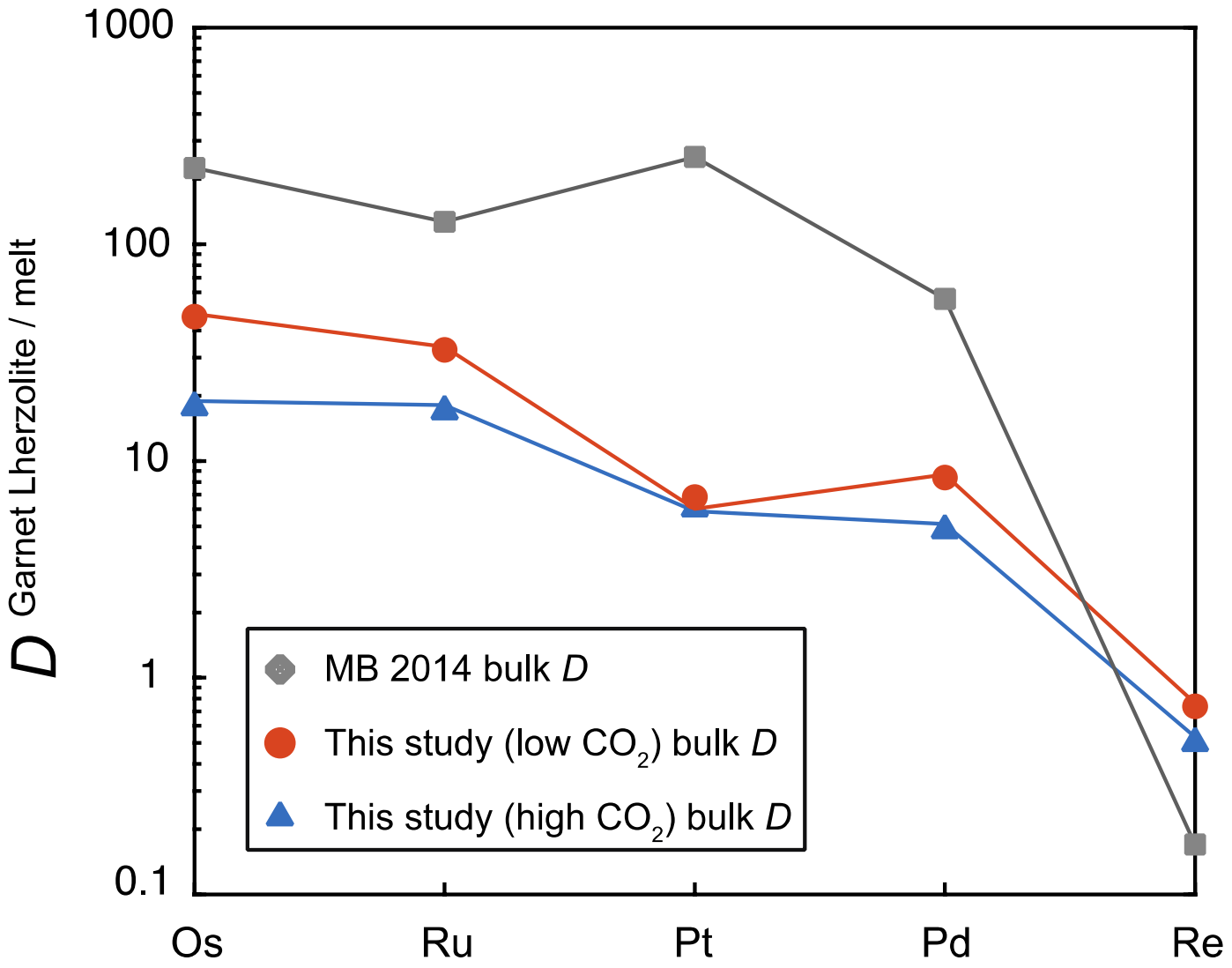

939

940 **Figure 4:** Bulk partition coefficients of HSEs applicable to carbonated melt generation from garnet
941 lherzolite. Orange symbols and line: low CO_2 melt (this study); blue symbols and line: high CO_2
942 melt (this study), and grey symbols and line [nominally CO_2-free, basaltic silicate melt; Mungall
943 and Brenan (2014)]. All plotted bulk D values are based on bulk sulfur content of 250 ppm,
944 assuming all sulfur is in the form of sulfide.

945

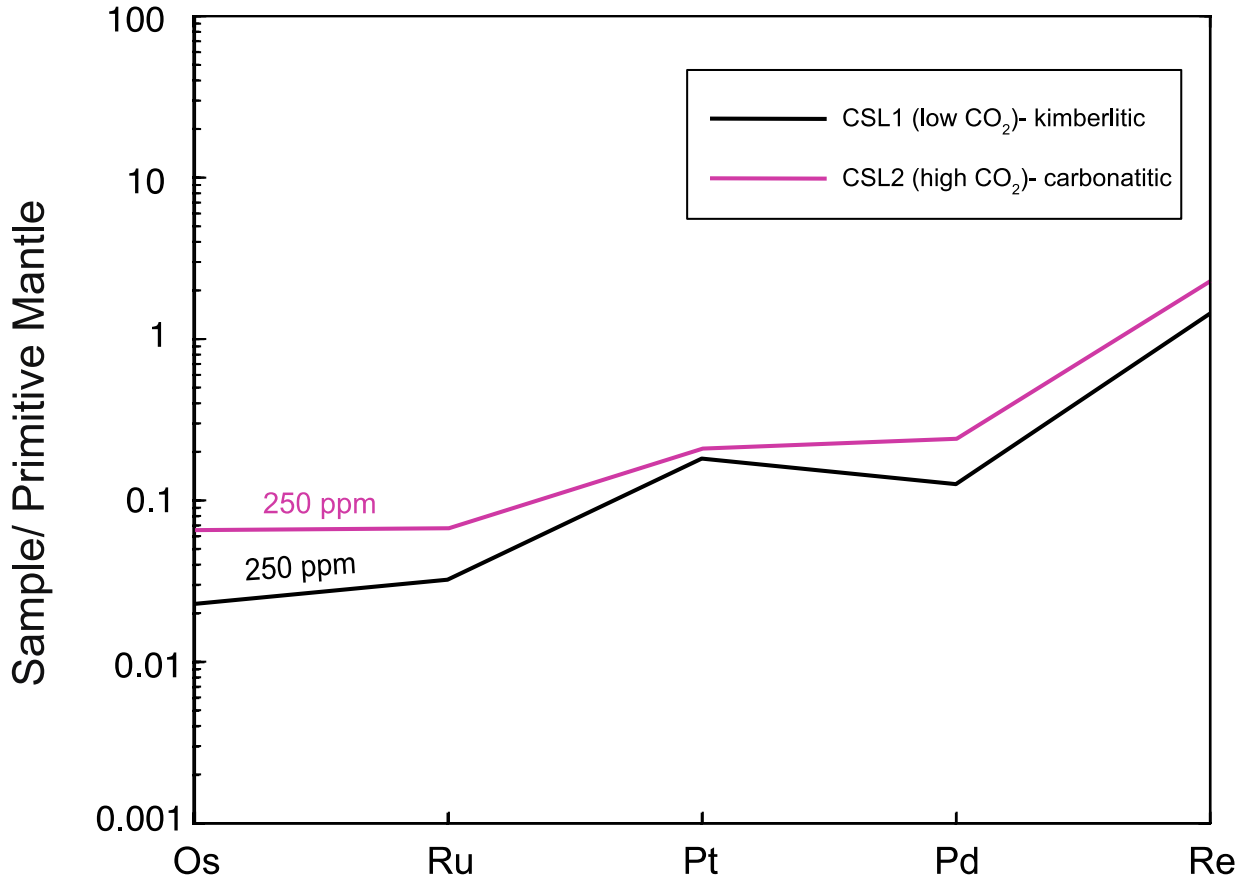

946

947 **Figure 5:** Primitive Mantle (PM) normalized HSE pattern of a kimberlitic and carbonatitic melt
948 assuming the primitive mantle is sulfide saturated and has 250 ppm S. Calculation is based on
949 bulk *D* for garnet lherzolite and for a low degree of melting of F=0.3 wt.% using the aggregate
950 fractional melting equation (1). I-PGEs (Os, Ru) are depleted in the melt whereas P-PGEs (Pt,
951 Pd) are enriched, indicating low I-PGE/P-PGE ratios for carbonatitic and kimberlitic melts.

952

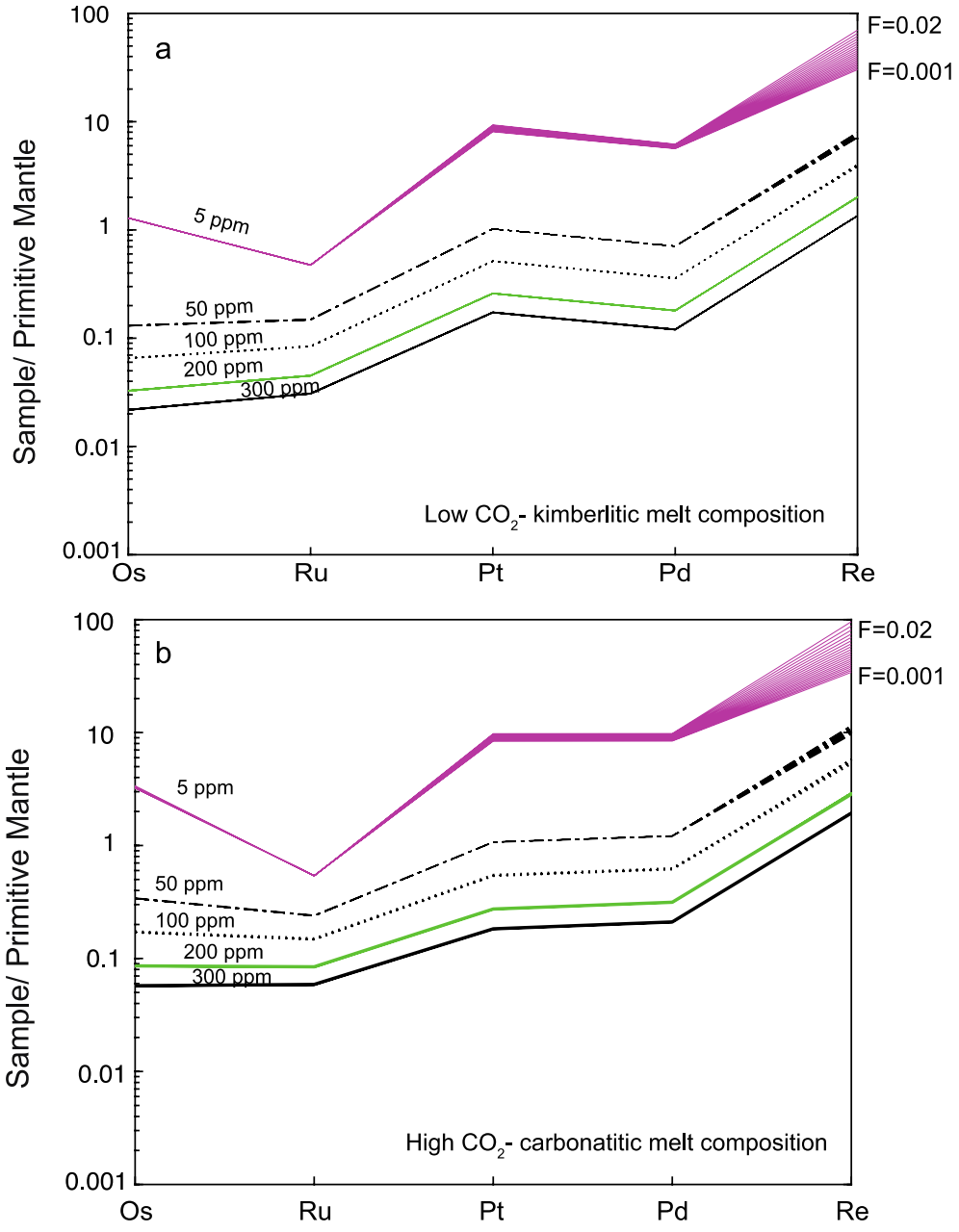

953

954 **Figure 6:** Primitive Mantle (PM) normalized HSE pattern for (a) kimberlitic (low CO_2) melt and

955 (b) carbonatitic (high CO_2) melt for a range of degree of melting (0.1-2 wt.%). The mantle is

956 sulfide saturated with S content varying from 5 to 300 ppm. The lower concentrations (lower end

957 of each thick line) for each bulk S content denote 0.1 wt.% melting and the higher concentrations

958 (higher end of thick lines) denote 2 wt.% melting.

959

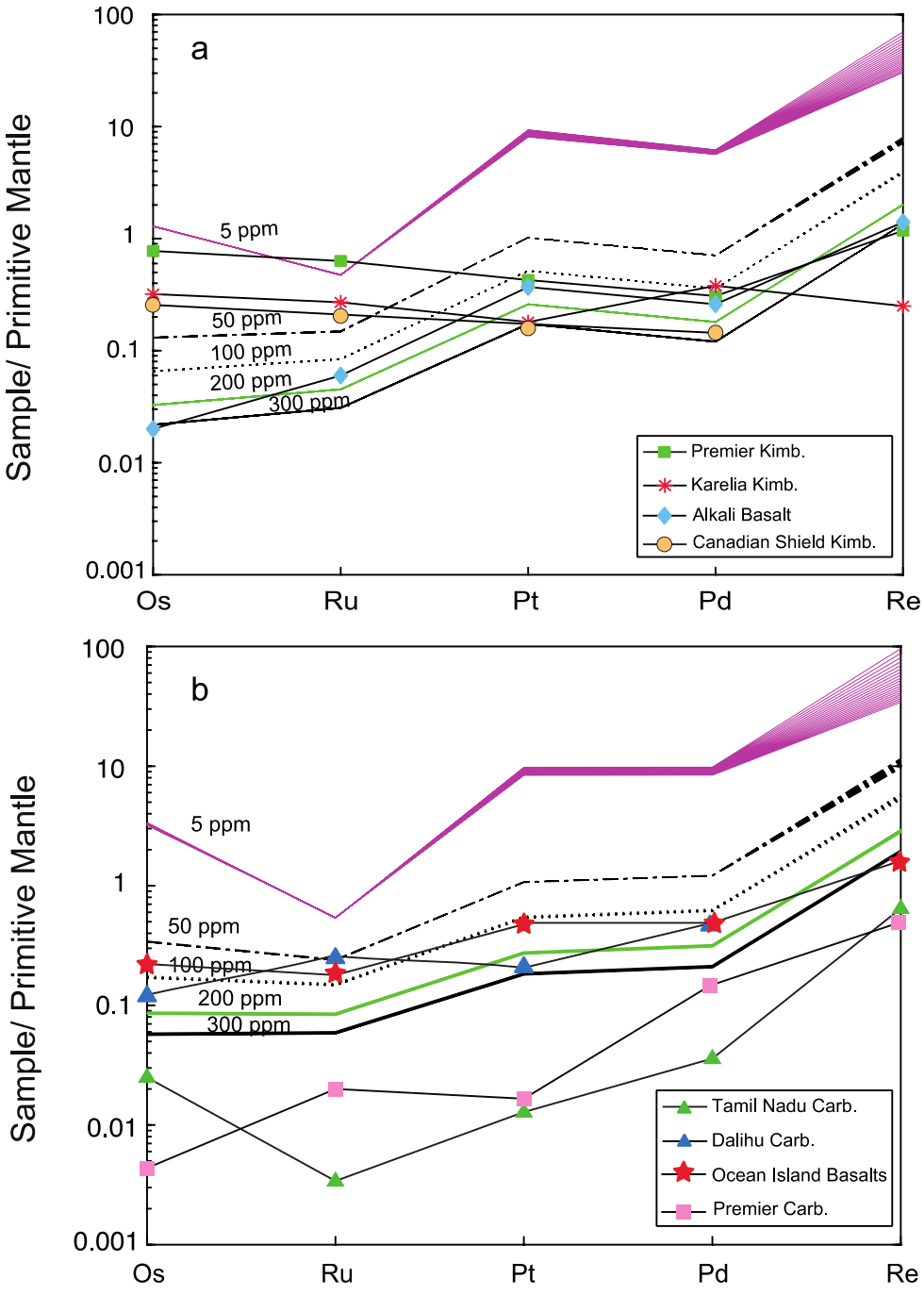

960

961 **Figure 7:** Primitive mantle normalized HSE pattern for (a) kimberlitic (low CO_2) melt and (b)

962 carbonatitic (high CO_2) melt for a range of degree of melting (0.1-2 wt.%). The mantle is sulfide

963 saturated with S content varying from 5-300 ppm. Also plotted in (a) are natural kimberlites from

964 Kaapvaal craton (Premier) (Maier et al., 2017), Karelia craton (Maier et al., 2017) and Canadian

shield craton (Tappe et al., 2017) and ocean island alkali basalt (Day et al., 2010). In (b) we also plot natural carbonatites from Dalihu, North China (He et al., 2020), Kaapvaal, South Africa (Tappe et al., 2020) and Tamil Nadu, India (Ackerman et al., 2019) along with Ocean Island Basalts (Day, 2013). We can see from the figure that the ocean island alkali basalt HSE patterns matches with a low degree kimberlitic melt of sulfide saturated mantle, whereas Ocean Island Basalts (OIBs) HSE pattern matches with a low degree carbonatitic melt of sulfide saturated mantle.

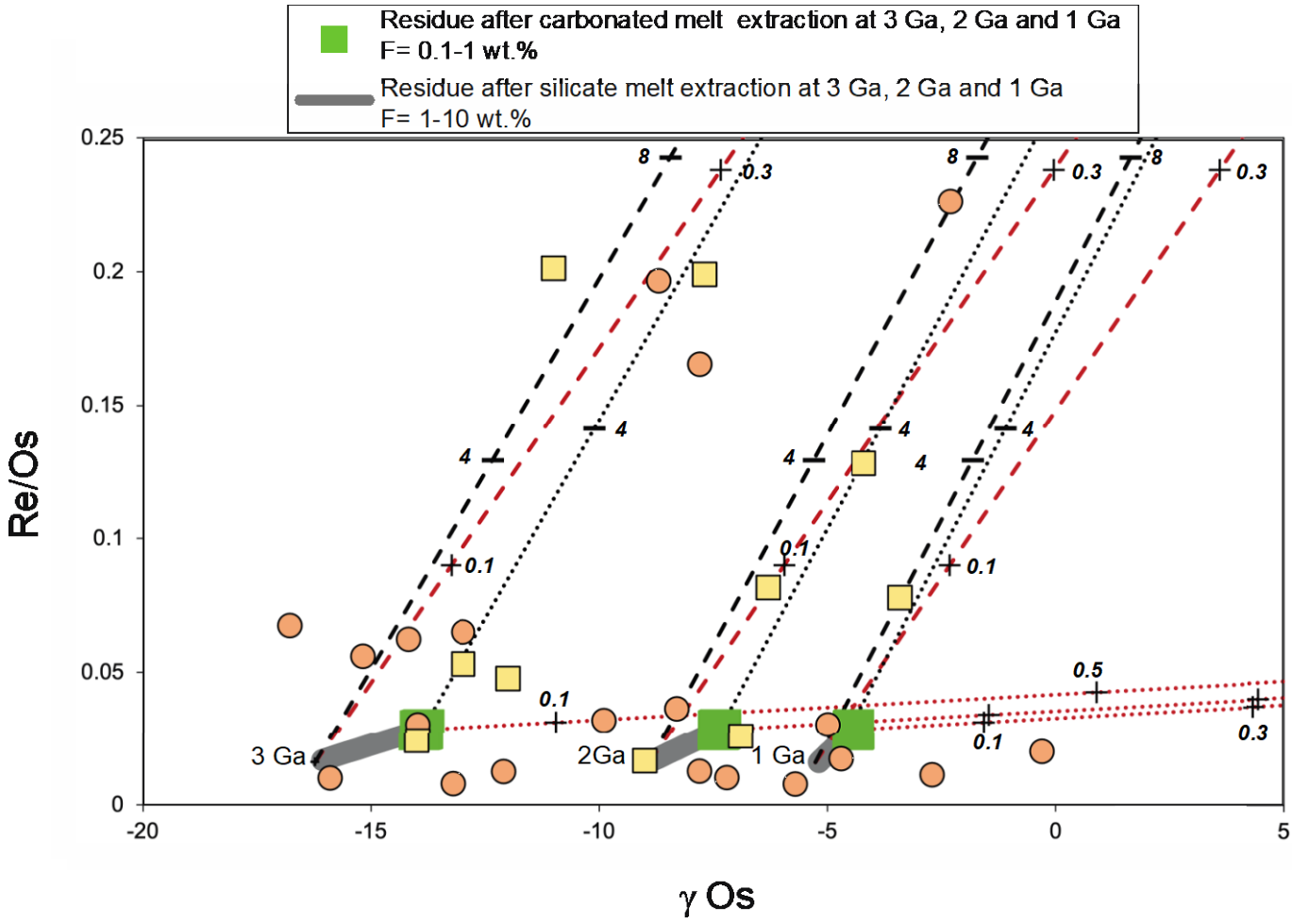

Figure 8: γ Os vs Re/Os plot for mantle xenoliths from Kaapvaal craton (orange circles) (Pearson et al., 1995) and Siberia (yellow squares) (Pearson et al., 1995) compared with models of carbonated or silicate melt depleted residue and carbonated melt addition (dashed black and dotted black lines) and silicate melt addition (dashed red and dotted red lines) based on the expected fractionation of Re-Os. Solid grey line shows the path of a residue after extraction of a silicate melt (1-10 wt.%) at 3 Ga, 2 Ga and 1 Ga. Green squares show a residue after extraction of carbonated melt (0.1-1 wt.%) at 3 Ga, 2 Ga, and 1 Ga. The black dashed line shows two-component mixing between 10 wt.% silicate melt extracted peridotite residue with a 0.5 wt.% carbonated melt extracted at 1 Ga, whereas the black dotted line shows mixing between 0.5 wt.% carbonated melt extracted peridotite residue with a 0.5 wt.% carbonated melt extracted at 0.5 Ga. The fractions of

melt component are indicated in italics. The red dashed line shows mixing between 10 wt.% silicate melt extracted peridotite residue with a 0.5 wt.% carbonated melt extracted at 1 Ga, whereas the red dotted line shows mixing between 0.5 wt.% carbonated melt extracted peridotite residue with a 0.5 wt.% carbonated melt extracted at 0.5 Ga. The fractions of melt component are indicated in italics. The carbonated melt and silicate melt extracted at 1 Ga is calculated using $(^{187}Os/^{188}Os)_{initial}$ = 0.1215 (Walker et al. 1989) for a primitive mantle.

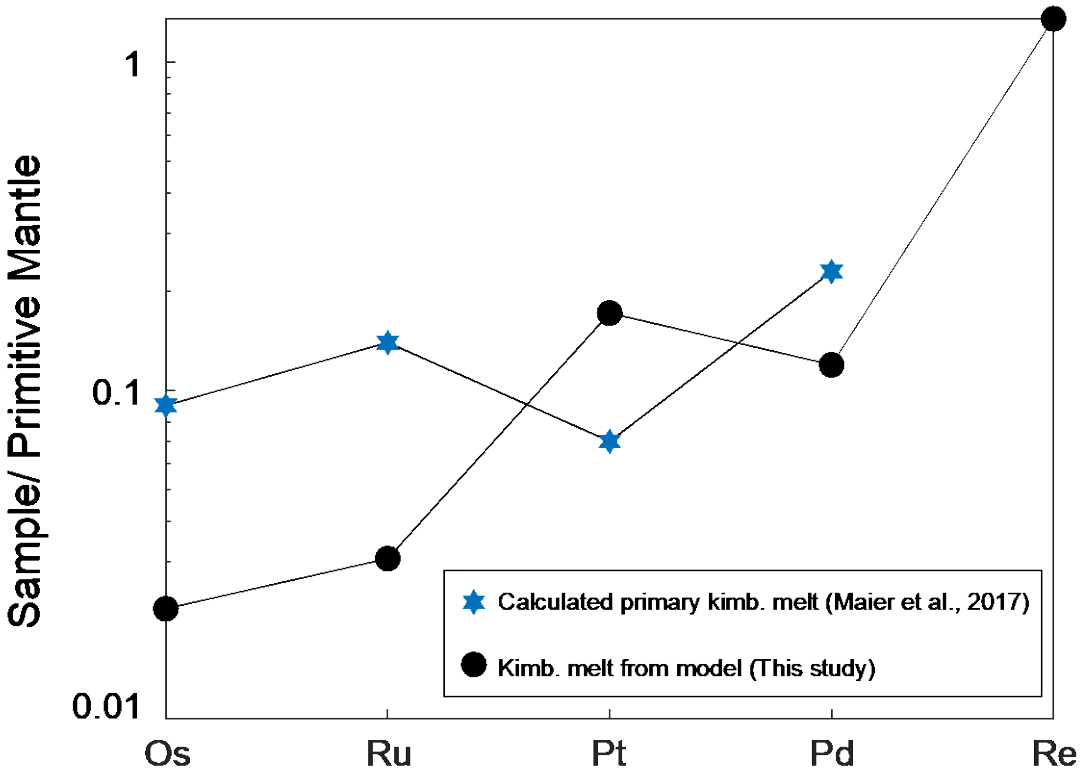

992

993 **Figure 9:** Primitive mantle normalized HSE content of a primary kimberlitic melt calculated by
994 mass balance using Ir concentrations (blue stars) by Maier et al. (2017) compared with a low
995 degree (0.3 wt.%) primary kimberlitic melt calculated using bulk *D* and aggregate fractional
996 melting equation from this study (black circles) for a sulfide saturated garnet lherzolitic mantle
997 with 250 ppm S.

998

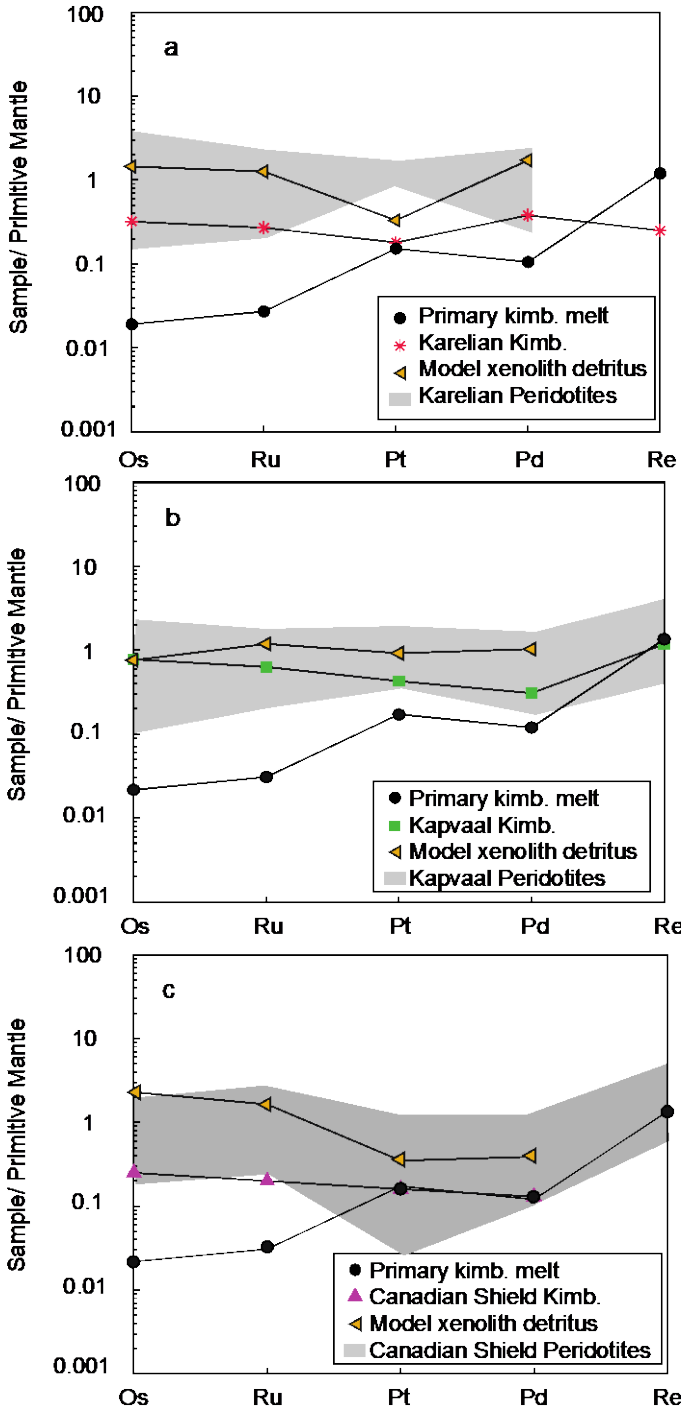

999

1000 **Figure 10:** PM normalized HSE pattern for natural kimberlite rocks from (a) Karelia (red stars),

1001 (b) Kaapvaal (green squares) and (c) Canadian shield Craton (violet triangles). Low degree (0.3

1002 wt.%) primary kimberlitic melt calculated using bulk *D* and aggregate fractional melting

1003 equation from this study (black circles) for a sulfide saturated garnet lherzolitic mantle with 250

1004 ppm S is plotted along with model SCLM detritus HSE contents (yellow triangles) which are
1005 calculated by mass balance using Ru concentrations. The PM normalized HSE pattern of the
1006 peridotitic xenoliths for these cratons are plotted as grey bands.

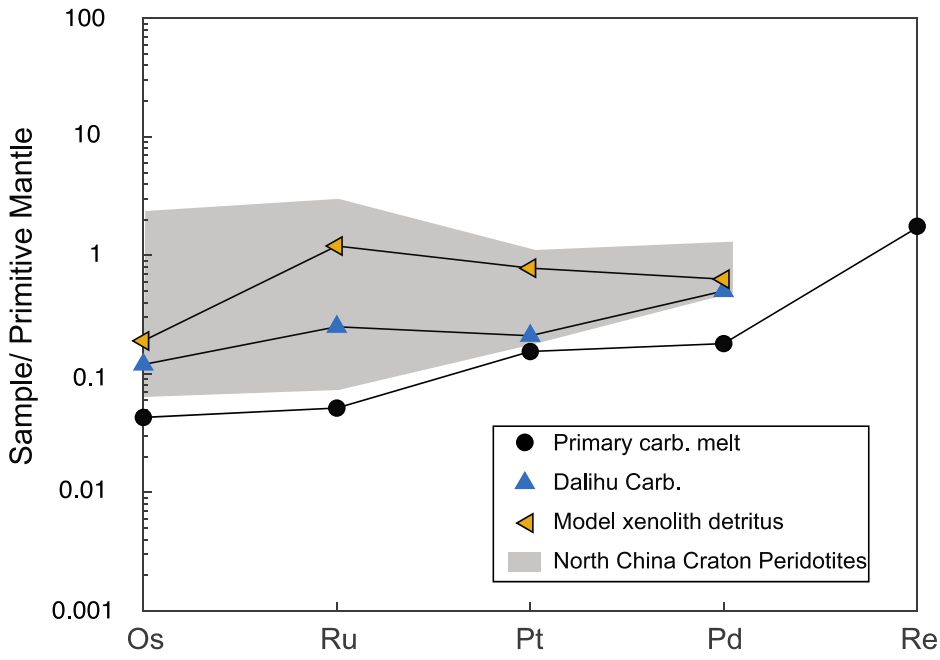

1007

1008 **Figure 11:** PM normalized HSE pattern for Dalihu carbonatite, North China (blue triangles).
1009 Low degree (0.3 wt.%) primary carbonatitic melt calculated using bulk *D* and aggregate
1010 fractional melting equation from this study (black circles) for a sulfide saturated garnet
1011 lherzolitic mantle with 250 ppm S is plotted along with model SCLM detritus HSE contents
1012 (yellow triangles), which are calculated by mass balance using Ru concentrations. The PM
1013 normalized HSE pattern of the North China Craton peridotitic xenoliths are plotted as grey
1014 bands.